

## DIPLOMA THESIS

# SMM Modeling and Capacitance Voltage Curves

Carried out at the

**Institute of Solid State Electronics  
at the Vienna University of Technology**

**and Agilent Technologies Linz**

supervised by

**Ao.Univ.Prof. Mag.rer.nat. Dr.rer.nat. Jürgen Smoliner**

and

**Dr. Ferry Kienberger**

Oliver Lang, BSc  
Matr.Nr.: 0627778

# Kurzfassung

Rastermikrowellenmikroskopie ist eine Messtechnologie am aktuellen Stand der Technik und Forschungsobjekt von vielen Forschungsgruppen auf der ganzen Welt. Es kombiniert die räumliche Auflösung eines Rasterkraftmikroskops mit der Signalprozessierung eines modernen Netzwerkanalysators. Diese zwei vollständig entwickelten Systeme eröffnen viele Möglichkeiten für zukünftige Anwendungen vielfältigster Art. Im Rastermikrowellenmikroskop wird ein Mikrowellensignal über Koaxialkabel hin zu einer leitfähigen Spitze des Rasterkraftmikroskops und weiter zu einer Probe geführt. Dort werden die Mikrowellen reflektiert. Das Verhältnis zwischen einfallender und reflektierter Mikrowellenleistung, Reflexionskoeffizient genannt, ist von den lokalen Probeneigenschaften abhängig.

Frühere Arbeiten versuchten eine Verbindung zwischen dem gemessenen Reflexionskoeffizienten und den lokalen Probeneigenschaften zu finden. Aber eine generell gültige und/oder benutzerfreundliche Verbindung konnte nicht gefunden werden. Eine Möglichkeit eine Verbindung herzustellen ist ein Ersatzschaltbild des Rastermikrowellenmikroskops aufzustellen. Solche Ersatzschaltbilder wurden in früheren Arbeiten entwickelt, kalibriert und analysiert anhand des Frequenzverhaltens. Aber sie wurden nie dazu benutzt um tatsächliche Messergebnisse in echte Probeneigenschaften umzuwandeln. Dies ist genau der Punkt an dem diese Arbeit beginnt.

In dieser Arbeit wurden existierende Ersatzschaltbilder modifiziert und erweitert. Die Ersatzschaltbilder wurden dann dazu benutzt um Messergebnisse in Probeneigenschaften umzuwandeln, welche wiederum mit Simulationsergebnissen verglichen wurden um die Gültigkeit der Ersatzschaltbilder zu testen. Zu diesem Zweck wurden physikalische Modelle von Metall-Isolator-Halbleiter Strukturen entwickelt und benutzt um die Korrektheit der Modelle zu überprüfen.

# Abstract

Scanning microwave microscopy is a state of the art measurement technology which is main topic of several research groups around the world. It combines the spatial resolution of an atomic force microscope with the signal processing capabilities of modern vector network analyzers. These two fully developed systems combined provide huge possibilities for future applications in many different fields of research. In the scanning microwave microscope, a microwave signal is guided via a conducting tip into the sample where it gets reflected. The ratio between the reflected and incident microwave power, denoted reflection coefficient, is dependent of the local sample properties.

Previous works tried to find a relation between the measured reflection coefficient and the local sample properties. But a general valid and/or user-friendly relation could not be found. One way to find a correlation between the measured reflection coefficient and the local sample properties is to build a lumped element model of the SMM. These models were investigated, calibrated and analyzed with the frequency sweep. But they were never used to transform some measurement data into sample properties. This is the starting point of this work.

In this work, the model attempts of previous works were reinvented and modified. The models then were used to transform measurement data into sample properties which further were compared with simulation results to test the validity of the models. For this purpose, a physical model of metal-insulator-semiconductor structures was invented and used to test the correctness of the models.

## Content

1	Introduction.....	4
1.1	Motivation/general idea.....	4
1.2	SMM setup.....	7
1.3	SMM measurement principle .....	8
2	Modelling of the SMM and sample .....	12
2.1	Theoretical capacitance voltage curves.....	13
2.1.1	MIS structure .....	13
2.1.2	Handling of the tip- and gold pad structure .....	22
2.1.3	Analysis .....	23
2.2	RLC model .....	23
2.3	Transmission line model .....	26
2.4	Model analysis and comparison .....	28
3	SMM Measurements and analysis.....	31
3.1	SMM Measurements .....	31
3.1.1	MC2 sample .....	31
3.1.2	Image measurements and conversion theory .....	32
3.1.3	S11(V) curve measurements.....	33
3.1.4	Measurement analysis.....	43
3.2	Data analysis using SMM models .....	45
3.2.1	Image conversion results .....	45
3.2.2	S11(V) curve conversion results.....	49
3.2.3	Investigation of the frequency dependency of the capacitance difference .....	53
3.3	Recapitulation of the conversion results .....	56
4	Conclusion .....	57

# 1 Introduction

## 1.1 Motivation/general idea

The scanning microwave microscopy (SMM) is a measurement method which combines the advantages of an atomic force microscope (AFM) and a microwave network analyser. The AFM allows very high spatial resolution due to the small tip sizes. The network analyser techniques are fully developed and allow extremely sensitive electrical measurements in the microwave field. Since microwaves have wavelengths in the centimetre area, the first guess would be that there is no way to measure in the nanometer scale. To make this possible the electrical field enhancement around sharp corners is used to locally penetrate a sample with microwaves. These microwaves get reflected at the sample. The ratio between the reflected and incident microwave power, denoted reflection coefficient, is dependent of the local sample properties. This allows very sensitive qualitative measurement of the local sample properties. Additional, many possible ways of investigation are possible, for example the dependency of the reflection coefficient on the measurement frequency, the bias voltage and many more. In [9], the influence of the tip geometry on the measurement results is shown by solving the two-dimensional Poisson equation, resulting in a function of the lateral spatial resolution in dependency of the tip diameter and the doping. In [10], an analytical model was invented which describes the amplitude and phase sensitivity of SMM measurements on metal-oxide-semiconductor structures. The amplitude and phase signal were calculated as a function of operation frequency, oxide thickness, tip radius, bias voltage, and doping concentration. [11] shows a similar investigation of the measurement frequency and the bias voltage with the difference that this work is focussed on  $dS_{11}/dV$  measurements. As one can already see, there are many ways of measuring with the SMM. And also many types of SMM setups exist.

The SMM setup used in this work is explained in 1.2. The preferred measurement type was chosen to be the bias voltage dependency of the reflection coefficient measured on metal-insulator-semiconductor (MIS) structures. The general idea behind this is to convert these measurement results into capacitance values, leading to the bias voltage dependency of the sample capacitance. This is also called capacitance voltage curve, or C(V) curve. The curvature of the C(V) curve gives deep insight into many different material properties [1]. The most important of these properties is the dopant concentration, but also the insulator thickness, oxide charges and interface traps of a MIS structure can be read out. This powerful measurement type opens the window into the semiconductor business. In modern semiconductor technology a measurement tool for the dopant concentration on the nanoscale is desired. The analysis of errors and the processing quality analysis would profit of such a measurement possibility.

C(V) curves in the nanoscale can also be measured using scanning capacitance microscopy (SCM). A deep insight into the basics of SCM gives [13]. The theory of the capacitance probe and its application to SCM are presented. A good practical application is shown in [14] and [15] including a discussion about the potential of this technique to show important probe-related phenomena. A good introduction into the different measurement types of SCM is given in [16] including a conversion formalism of the SCM data into doping concentration values. In [17], the influence of several parameters in SCM measurements as such as the bias voltage is shown. It turned out that a non-zero bias voltage improves the lateral

resolution as well as the dopant resolution. [18] illustrates the physical limitations of SCM using two- and three-dimensional simulation of the measurement process. Also, a comparison of the SCM technique with the competitive scanning spread resistance microscopy (SSRM) technique is presented. In [21], a slightly different way of measuring the dopant concentration with an SCM is presented. With a feedback loop, the magnitude of the ac bias voltage applied to the sample is adjusted in a way so that one obtains a constant capacitance change as the tip scans across the sample surface. The general drawback of the SCM measurement is that it takes long time to measure the capacitance voltage curves compared with the SMM.

The SMM fulfills the requirements for measuring the dopant concentration on the nanoscale and in short time. An applied bias voltage changes the sample capacitance of a MIS sample. This changes the reflection coefficient of the tip/sample structure which can be measured by the PNA. The goal is to use the models to convert the measured bias voltage dependency of the reflection coefficient into C(V) curves. These C(V) curves are then used to read out the dopant concentration of the underlying semiconductor.

But not only would the semiconductor industry profit from such a measurement tool. For example the biology sector could use the capacitance values measured on biological samples for further analysis. The measurement of the thickness of lipid layers, membranes and other structures would be possible with a correct sample model. Also the dielectric constant of many different structures and also liquids could be measured. An expertise and overview of these applications can be found in [2]. There, the same setup was used as for this work. Based on this setup, several types of measurements were discussed. [19] shows the limitation of the spatial resolution and of the sensitivity when measuring dielectric constants. The dielectric properties of cells and their components in the context of biotechnology measurements in the radiofrequency range can be found in [20].

All these possible applications are based on a correct conversion of the measured reflection coefficient into sample capacitance values. This can be done with a quantitative model. The historical perspectives and fundamental physics involved in this field can be found in [22]. In [5], a model of the SMM was invented using antenna theory. The radiating electromagnetic waves around the tip were simulated by a point-like dipole. Then, Green functions were used to describe the electrodynamic response of the tip/sample system. Again on the same setup as it was used for this work, calibrated capacitance-voltage curves as well as derivative  $dC/dV$  curves were measured on samples with varying doping concentrations in [7]. Then the change of the capacitance and  $dC/dV$  curve was linearly connected with the doping concentration which provides a quantitative connection between the measured reflection coefficient and the doping concentration. A preview of the possible measurement sensitivity with this setup is illustrated in [8]. In that paper, MIS structures with different sized gold contacts on  $\text{SiO}_2$  layers with different thicknesses were acquired and converted with the same calibration method as in [7]. The results were compared with measurements performed at an external capacitance bridge. Approach curves were used to determine the cantilever stray capacitance. Measurements at 1GHz with a shielded cantilever were performed in [12]. Approach curves were used to measure the dielectric constant of bulk samples which then were compared with simulation results.

Another possible way of converting the measurement data is to find a correct lumped element model of the SMM. This attempt is not new. A lumped element model was invented in [3]. But the model was only tested by comparing the frequency behavior of the model and the SMM, followed by some investigation of the sensitivity and other properties. But the model was never used to convert real measurement data, for example the voltage dependency of the reflection coefficient, into capacitance data, leading to C(V) curves. This is the point this work is focused on.

In this work, two different lumped element models were invented. They were designed to imitate the electrical microwave design of the SMM setup. Every lumped element models has its unknown elements. They need to be defined first. This is been done by taking a look at the frequency behavior, denoted frequency sweep. Such a frequency sweep can be measured between 1GHz and 20Ghz. And of course, it can be simulated with the two models. A comparison between the modeled frequency sweep and the measured frequency sweep delivers the right values for the unknown elements of the models. A program was invented which changes the values of the unknown elements till the two frequency sweeps overlap. With the complete models, several forms of analysis were performed. Then the complete models were used to transform measured images and measured voltage bias sweeps into sample capacitance values. The results were compared with simulation results to test the validity of the models.

As a test sample, metal-insulator-semiconductor (MIS) structures were chosen. A sample called the 'MC2 sample' provides several different shaped gold pads on several insulator steps. The underlying semiconductor is n doped silicon. A physical model was invented which calculates the voltage dependent sample capacitance including the depletion zone capacitance. The results from the physical model were compared with the conversion results from the SMM models.

## 1.2 SMM setup

The setup can be divided into two main parts, Agilent's atomic force microscope (AFM) and Agilent's performance network analyser (PNA) (Figure 1.1). The AFM includes a scanner (Figure 1.2), which moves a cantilever with a nanoscopic tip over the surface of a probe. The cantilever and the tip are made of conducting platinum which allows applying a voltage to the probe via the tip. On the other side, the cantilever is connected via several coaxial cables to the PNA. The PNA sends out an electromagnetic wave with a frequency between 1 and 20GHz and detects the incoming reflected signal. These frequencies are in the microwave range hence the name Scanning Microwave Microscopy (SMM).

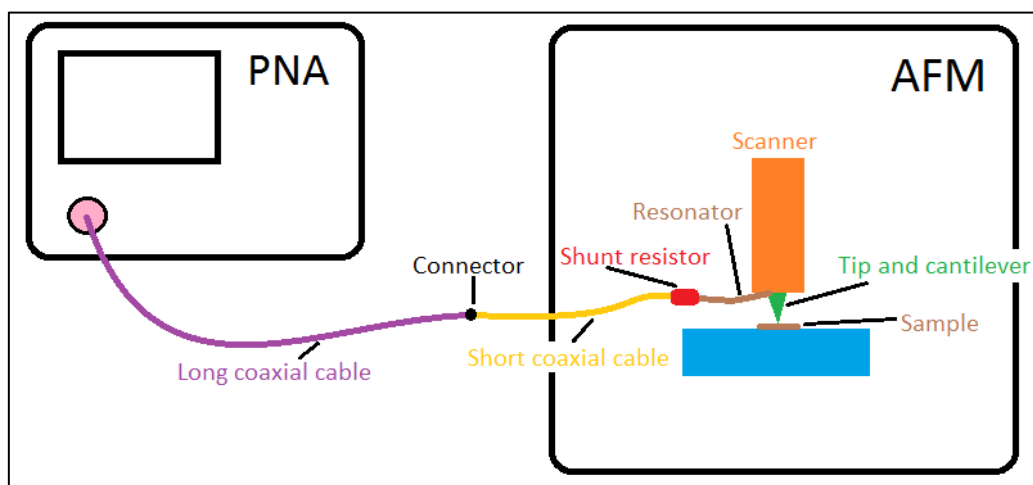


Figure 1.1: Schematic drawing of the SMM setup. The two main parts are the atomic force microscope (AFM) and Agilent's performance network analyser (PNA) which is connected via several coaxial cables.

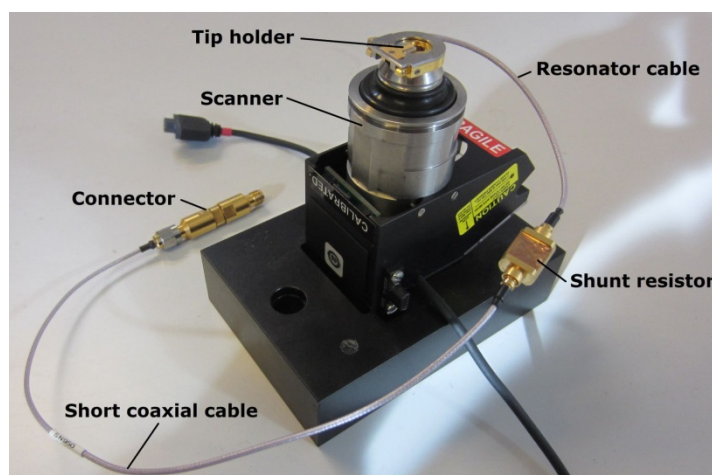


Figure 1.2: Scanner and electrical wires of the setup. Visible are the coaxial cables from the connector to the tip including the shunt resistor.

When dealing with microwaves and coaxial cables, one can obtain reflections at every non-ideality. Every connector produces reflections and even every bending of the cable changes its electromagnetic properties. By taking a look at the schematic drawing of the measurement setup in Figure 1.1 one can imagine that there occur reflections at the connector between the long coaxial cable and short coaxial cable, the shunt part including the 50Ω shunt resistor, and the cantilever/tip part. The wavelength in the cable is roughly between 1 and 20 cm so we consider there is only one main reflection at the cantilever/tip system because the dimensions are way smaller than 1 cm. The PNA calculates the reflection coefficient  $\Gamma$  of the system connected to its port. It displays the amplitude of the reflection coefficient on a logarithmic scale according to

$$\begin{aligned} \text{Amplitude}(S_{11}) &= 20 \cdot \log|\Gamma| && \text{(Error! Style not defined..1)} \\ \text{Phase}(S_{11}) &= \text{angle}(\Gamma). && \text{(Error! Style not defined..2)} \end{aligned}$$

S11 means the signal is sent out on port 1 and detected also on port 1. Hence, S11 means the reflection coefficient on a logarithmic scale.

### 1.3 SMM measurement principle

The PNA allows measuring the reflection coefficient in dependence of the frequency for a broad frequency spectrum. A frequency sweep (Figure 1.3) gives a better insight into the cable setup.

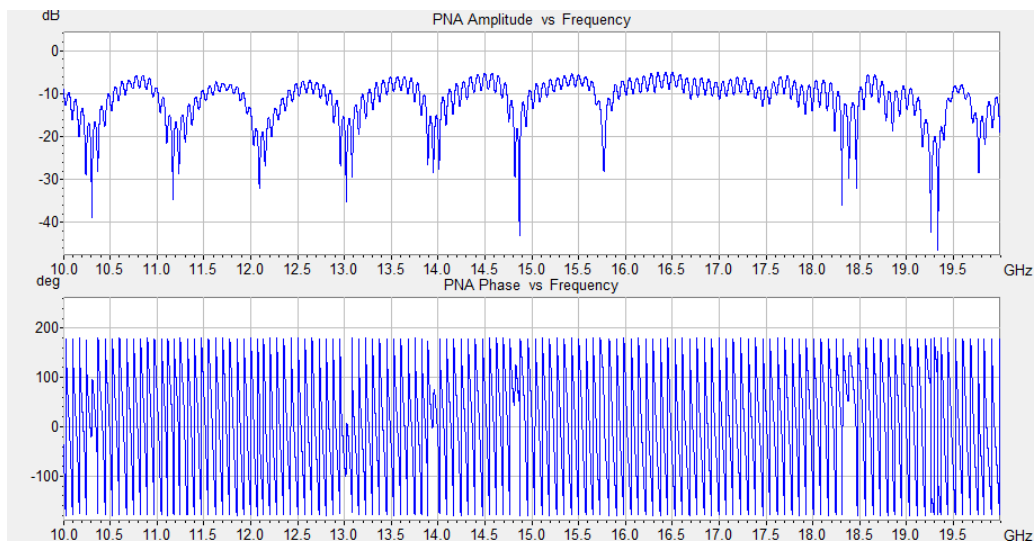


**Figure 1.3: Uncalibrated frequency sweep from 10GHz to 20GHz. The upper window shows the PNA amplitude and the PNA phase is shown in the lower window.**

The resonance frequencies occur periodically. The big resonance peaks every 900MHz occur due to the 6 cm long resonator cable (brown in Figure 1.1). The smaller resonance peaks every 70 MHz arise from the

1 meter long coaxial cable (purple in Figure 1.1). In this frequency sweep, the influence of the short coaxial cable (yellow in Figure 1.1) is not significant.

Using the electronic calibration (E-Cal) module from Agilent (Figure 1.5), the PNA can mathematically remove the long coaxial cable. After this, the frequency sweep changed (Figure 1.4).

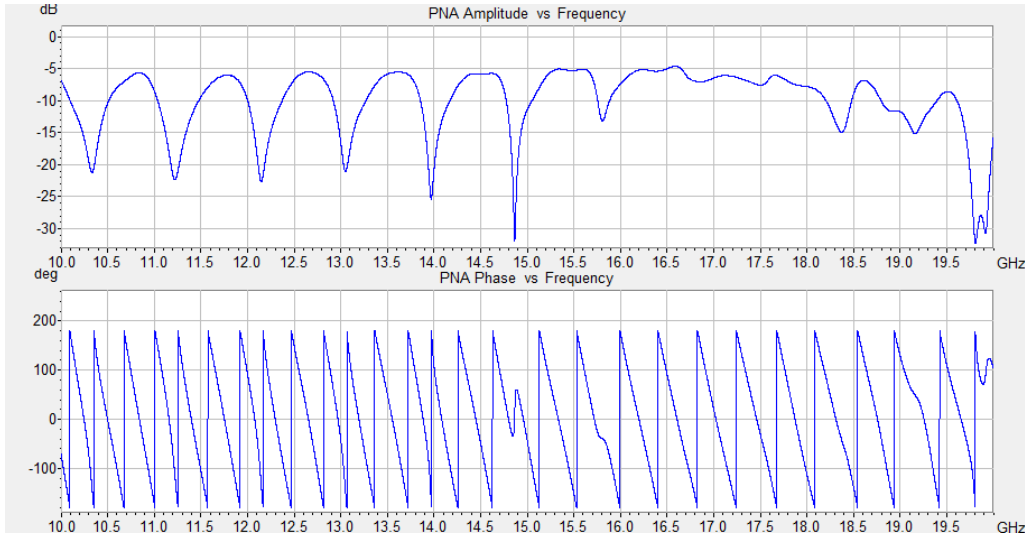


**Figure 1.4: Calibrated frequency sweep from 10GHz to 20GHz. The upper window shows the PNA amplitude and the PNA phase is shown in the lower window.**



**Figure 1.5: Agilent's electronic calibration module (E-Cal module) allows a mathematical removal of coaxial cables from the setup.**

The small resonance peaks every 70MHz disappeared. What stays are the resonance peaks every 900MHz due to the resonator cable. The short coaxial cable (yellow in Figure 1.1) causes the periodical phase curvature with a period of approximately 300MHz. Also, this short coaxial cable is mostly responsible for the unsymmetrical amplitude curvature at the right half of the spectrum (Figure 1.4).

Such measurements where the long coaxial cable is mathematically removed, denoted calibrated measurements, are preferable when it comes to interpret the measured  $S_{11}$  values. In fact, all measurements in this work were calibrated measurements.

One can see every coaxial cable acts as a resonator. The last coaxial cable between the  $50\Omega$  shunt resistor and the cantilever/tip/sample system is the main resonator which causes the good visible deep resonance minima. The depth and the frequency of the resonance minima are dependent of the complex impedance of the sample because the cantilever/tip/sample system acts as a terminating impedance of the resonator cable. If we choose a measurement frequency in the very near of such a resonance peak and stick to this measurement frequency, the reflected signal changes according to the local sample properties. This changing  $S_{11}$  parameter can be measured. With this setup it is possible to scan samples, perform several sorts of sweeps including the frequency sweep and a DC voltage sweep.

Figure 1.6 shows an example of such a calibrated frequency sweep between 1 and 15GHz. The resonance minima were numbered from 1 to 14. One can recognize that the phase at the resonance minimum is sometimes falling and sometimes rising.

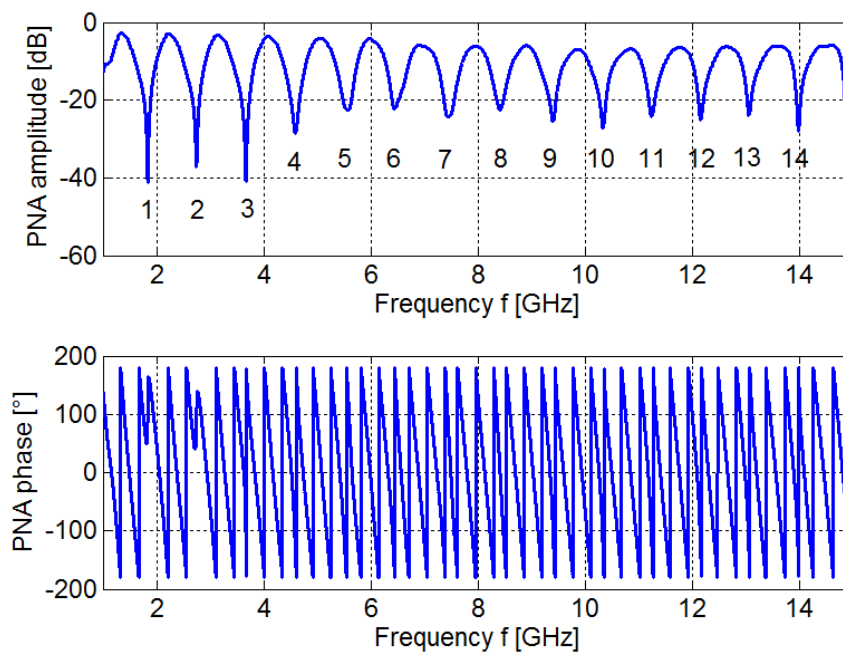


Figure 1.6: Calibrated frequency sweep between 1 and 15GHz. The upper window shows the measured PNA amplitude signal and the lower window shows the measured PNA phase signal. The resonance minima were numbered from 1 to 14.

To investigate the underlying behaviour in the complex plane, certain resonance minima were plotted in the complex plane (Figure 1.7).

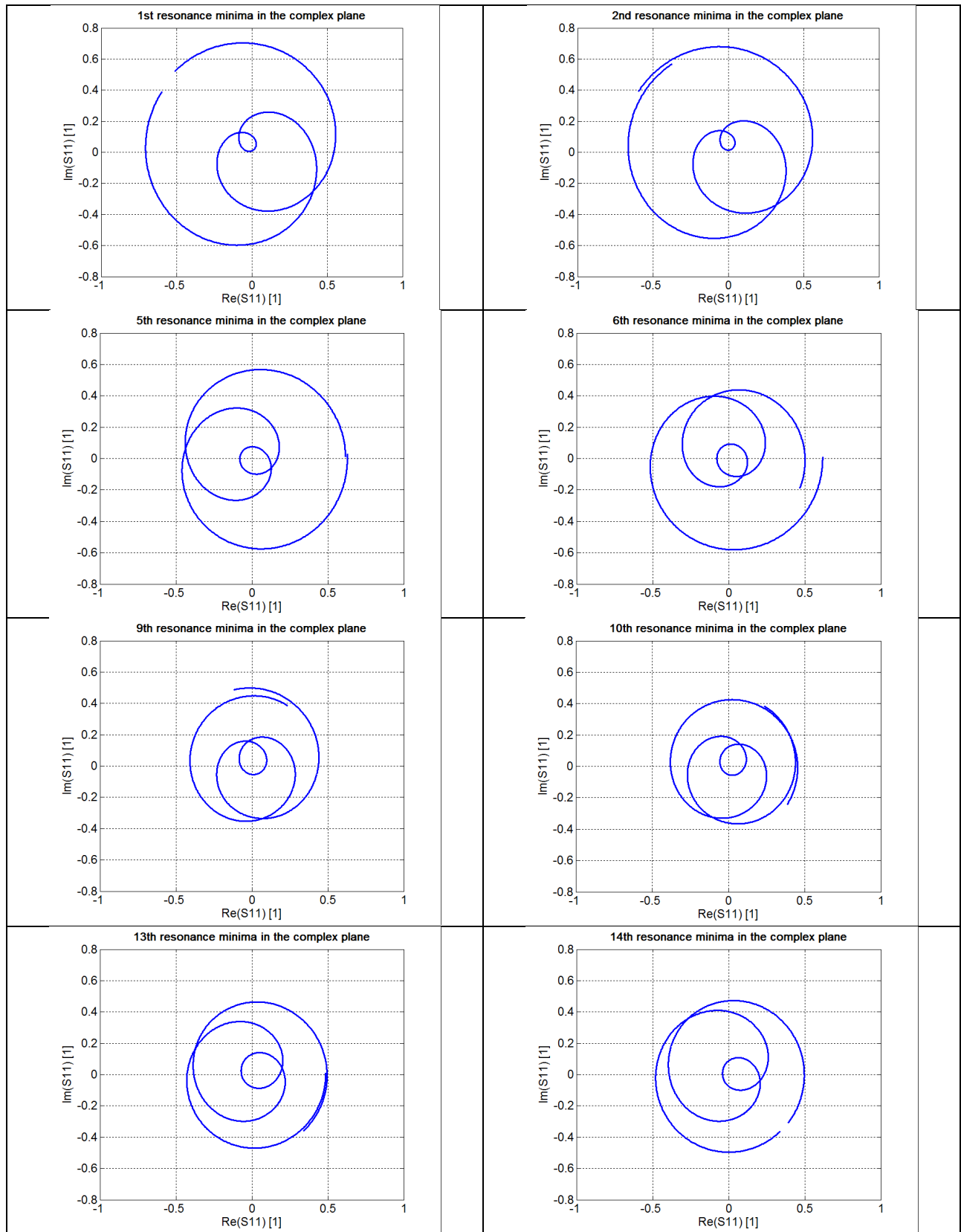


Figure 1.7: Smith chart of the resonance minima with the number 1, 2, 5, 6, 9, 10, 13 and 14 according to the numeration in Figure 1.6.

The only difference between resonance curves with falling/rising phase at the resonance minimum is, that the resonance curve is encircling/not encircling the zero point. With an ideal resonator and without any additional coaxial cable, all these curves would lie on top of each other. If one would remove the short coaxial cable (yellow in Figure 1.1), every resonance minima has only one circle in the complex plane instead of three.

## 2 Modelling of the SMM and sample

The SMM combines a very high spatial resolution with a high sensitivity in a broad frequency spectrum. A problem which still remains is that it is difficult to read out sample properties out of the measured complex  $S_{11}$  values.

There are two general ways which can be used for a calibration. The first one is to find a connection between the complex  $S_{11}$  parameters and certain spots on the sample where the electrical properties are already known. The first one is called 'Black Box calibration' and was invented and published by Johannes Hoffmann et al. [6] in 2012. It is a way to calibrate images measured with the SMM but it also has its limitations. To do this calibration, a connection between the complex  $S_{11}$  parameter and the local sample properties is made on three different spots on one scanned image. This connection between the complex  $S_{11}$  parameter and the sample capacitance leads to the ability to convert the rest of the image into capacitance values to. A drawback of this method is that one has to know the electrical properties of the sample on three different spots in order to convert the rest of the sample. The second way is to use the frequency sweep and calibrate a lumped element model of the SMM with it.

This work deals with the second way. Two different attempts of modelling the electric properties of the SMM are shown in this chapter. This work is focused on two applications of the SMM: the normal  $S_{11}$  image measurement, and the voltage dependent  $S_{11}(V)$  measurement on semiconductor capacitors. With the models, one can convert the  $S_{11}(V)$  measurements into capacitance voltage curves, which are very common in the semiconductor industry as a source of various sample properties. Both applications allow a controlling of the modelling attempts by comparing the capacitance results with those of physical simulation. First, the derivation and results of the voltage dependent capacity of semiconductor samples are shown. After that, the two models are presented followed by a short introduction of the Black Box calibration algorithm.

## 2.1 Theoretical capacitance voltage curves

The samples which were measured with the SMM in this work were Gold/Oxide/semiconductor structures which form a capacitor with one contact being a gold pad and the other contact being the doped silicon sample (Figure 2.1).

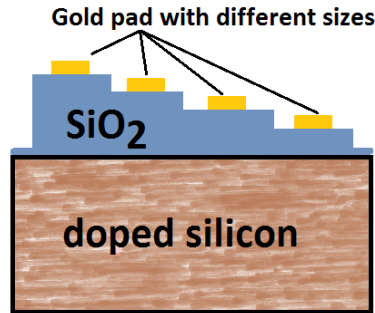


Figure 2.1: Schematic drawing of the samples structure.

While scanning, when the tip is in contact with the gold pad one can say a capacitor is connected with the tip. When the tip touches the oxide, the tip itself builds the metal contact of the capacitor. From the modelling point of view, it all comes down to a Metal-Insulator-Semiconductor (MIS) structure (Figure 2.2). This chapter deals with the formula background and theoretical analysis of MIS structures. The goal is to find a general valid formula which describes the capacitance voltage curves on any kind of sample.

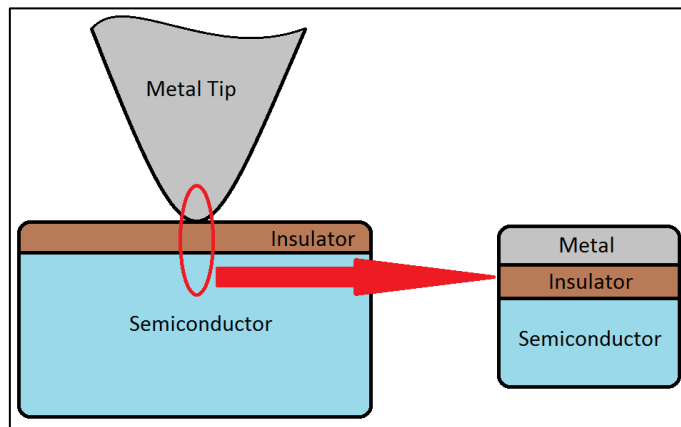


Figure 2.2: Schematic drawing of the tip/insulator/semiconductor structure.

### 2.1.1 MIS structure

The first step is to take a detailed look at the band diagram of such a MIS structure. Figure 2.3 shows the band structure at equilibrium, i.e. when no voltage is applied.

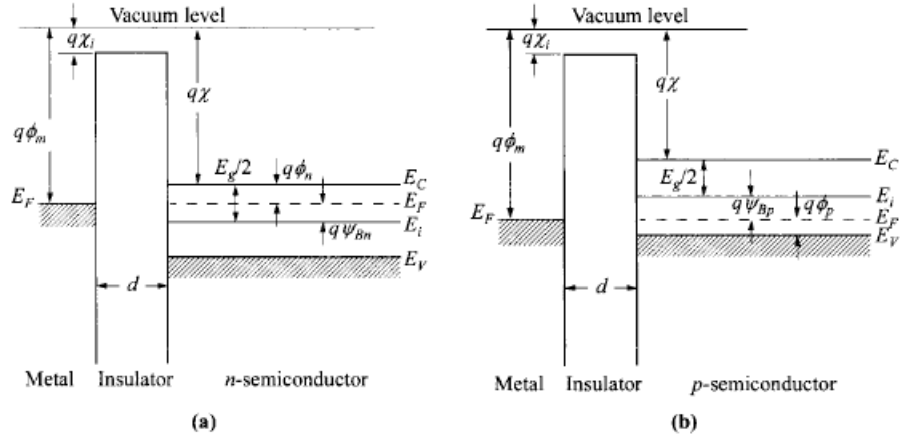


Figure 2.3: Energy-band diagrams of ideal MIS capacitors with no voltage applied for a n-type semiconductor (a) and a p-type semiconductor (b). Image taken from [1].

An applied voltage affects the carriers in the semiconductor. They can be attached or detached to the semiconductor insulator interface caused by a band deflection in the affected area. One can calculate the electron and hole density via this band deflection. From now on, we only consider the surface potential on the edge of the semiconductor and neglect the metal and the insulator. They will be reintroduced later on. So,  $\Psi_s$  is the surface potential of the semiconductor, and  $\Psi_p(x)$  is the potential in an arbitrary point with respect to the bulk of the semiconductor. Later, the surface potential of the semiconductor will be calculated out of the applied voltage and the potential drop in the insulator.

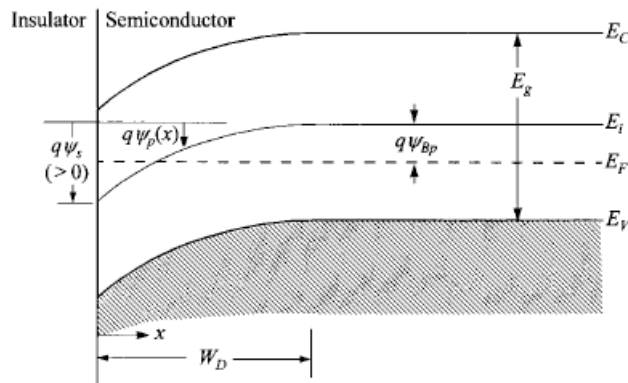


Figure 2.4: Energy-band diagram at the surface of a p-type semiconductor with positive surface potential. Image taken from [1].

The formula for the potential in an arbitrary point in the semiconductor (Error! Style not defined..1) can be directly derived from Figure 2.4.

$$\Psi_p(x) = -\frac{E_i(x) - E_i(\infty)}{q} \quad (\text{Error! Style not defined..1})$$

In Figure 2.4 the depletion width  $W_D$  is indicated as the length of the band bending. The Fermi level indicates a p-type semiconductor which is the main semiconductor type for which the derivation of the

formulas is shown. By changing the signs of the voltages and potentials one can make the formulas valid for n-type semiconductors.

As mentioned above, the electron and hole densities ((Error! Style not defined..2) and (Error! Style not defined..3)) can be calculated from the bending of the band structure. Boltzmann statistic is sufficient.

$$n_p(x) = n_{p0} e^{\frac{q\Psi_P}{kT}} = n_{p0} e^{\beta\Psi_P} \quad (\text{Error! Style not defined..2})$$

$$p_p(x) = p_{p0} e^{-\frac{q\Psi_P}{kT}} = p_{p0} e^{-\beta\Psi_P} \quad (\text{Error! Style not defined..3})$$

$\beta$  is just an abbreviation and stands for  $q/kT$  which is one over the temperature voltage.  $n_{p0}$  and  $p_{p0}$  are the equilibrium electron and hole densities. Considering a doped semiconductor they can be calculated via the doping density and the intrinsic carrier density  $n_i$  of the semiconductor.

		n type semiconductor	p type semiconductor
Electron density	n	$n_{n0} \approx N_D$	$n_{p0} \approx n_i^2/N_A$
Hole density	p	$p_{n0} \approx n_i^2/N_D$	$p_{p0} \approx N_A$

By varying the surface potential and taking a look at the electron and hole densities ((Error! Style not defined..4) and (Error! Style not defined..5)) one can distinguish three different main states and two intermediate states.

$$n_p(0) = n_{p0} e^{\beta\Psi_s} \quad (\text{Error! Style not defined..4})$$

$$p_p(0) = p_{p0} e^{-\beta\Psi_s} \quad (\text{Error! Style not defined..5})$$

The three main states are called accumulation, depletion and inversion. The proper band diagrams are shown in Figure 2.5. To cover up p- and n-type semiconductor samples the minority and majority carriers are handled instead of electrons and holes.

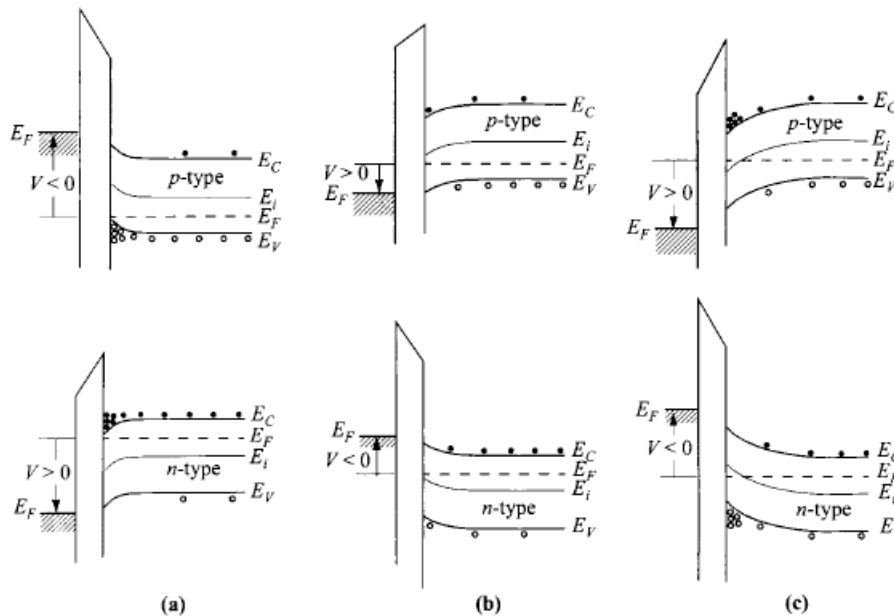


Figure 2.5: Energy-band diagrams of the accumulation (a), depletion (b) and inversion (c) state. Image taken from [1].

Accumulation means an enhanced concentration of majority carriers in the close area of the semiconductor insulator interface. This is the case for an n-type semiconductor at positive surface potentials and vice versa. When reducing the surface potential towards zero, accumulation becomes weaker and finally disappears. When the surface potential  $\Psi_s$  is zero one obtains the standard unbiased charge densities of the bulk semiconductor. This special case is called flat-band condition due to the horizontal energy bands (Figure 2.3) and is one of the two intermediate states. Another special case exists where the majorities are pushed away without attracting the minority carriers. This case is called depletion and it occurs at slightly positive/negative surface potentials for p/n-type semiconductors. This case leads to carrier depletion near the insulator semiconductor interface. In the other direction of the surface potential scale one obtains an inversion of the carrier concentration. The minorities are attracted by the surface potential  $\Psi_s$ , rise in number and become finally the majorities in this area. This case is called inversion. A differentiation between weak and strong inversion is useful. To do this, a certain surface potential value at which the intrinsic energy level at the surface is equal to the Fermi energy level is defined. This certain surface potential value shall be called  $\Psi_{Bp}$ . One can equally say that  $\Psi_{Bp}$  is the difference between Fermi potential and the intrinsic potential (Figure 2.4). One obtains weak inversion if the surface potential  $\Psi_s$  is between  $\Psi_{Bp}$  and  $2\Psi_{Bp}$ . Weak inversion means a minority carrier enhancement. Near the surface, the amount of minorities becomes bigger than the amount of majorities. Strong inversion can be obtained if the surface potential becomes bigger than  $2\Psi_{Bp}$ . Then, the amount of minorities near the surface becomes bigger than the amount of majorities in the bulk of the semiconductor. Table 2.1 sums up all discussed states and special surface potential values for a p type semiconductor.

**Table 2.1: States and proper surface potential values for p type semiconductors.**

Surface potential	State
$\Psi_s < 0$	Accumulation
$\Psi_s = 0$	Flat-band case
$\Psi_{Bp} > \Psi_s > 0$	Depletion (detracting of holes)
$\Psi_s = \Psi_{Bp}$	Fermi level at intrinsic level
$2\Psi_{Bp} > \Psi_s > \Psi_{Bp}$	Weak inversion
$\Psi_s > 2\Psi_{Bp}$	Strong inversion

With an electrical voltage at the metal contact of a Metal-Insulator-Semiconductor structure one can influence the carriers in the semiconductor. A relative high voltage in the positive or negative direction ( $|U| > 1V$ ) attracts minority or majority carriers towards the insulator semiconductor interface yielding in a state where this huge amount of carriers is separated by the insulator from the huge amount of carriers in the metal layer. This is similar to an ordinary capacitor and can be handled as this. A schematic drawing of this for positive voltages can be seen in Figure 2.6.

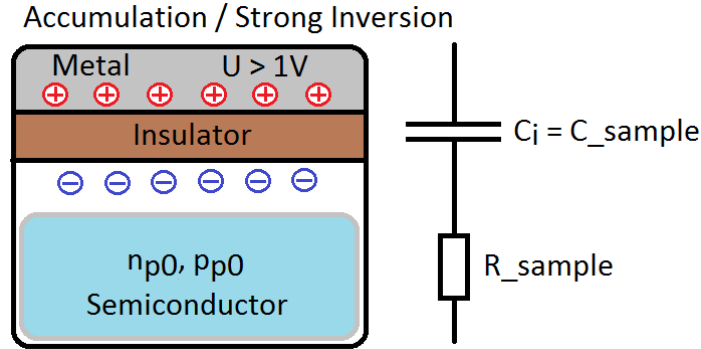


Figure 2.6: Schematic drawing of the carrier clouds in a MIS structure at positive voltages and the proper lumped element model.

It is useful to speak about capacitance per unit area instead of capacitance since no geometrical information is needed. The insulator capacity per unit area  $C_i$  is simply (Error! Style not defined..6).

$$C_i = \frac{\epsilon_i}{d} \quad (\text{Error! Style not defined..6})$$

This covers the accumulation and the strong inversion state. The weak inversion and the depletion cases are way more complex.

From (Error! Style not defined..2) and (Error! Style not defined..3) one can calculate the electron and hole densities in the semiconductor as a function of the surface potential. With these values one gets the space charge density by including the doping and multiplying with the elementary charge (Error! Style not defined..7).

$$\rho(x) = q(N_D^+ - N_A^- + p_p - n_p) \quad (\text{Error! Style not defined..7})$$

This space charge density delivers information about the potential in the semiconductor by solving the Poisson equation (Error! Style not defined..8).

$$\frac{d^2\Psi_P}{dx^2} = -\frac{\rho(x)}{\epsilon_S} \quad (\text{Error! Style not defined..8})$$

The Poisson equation needs two boundary conditions which are simply the surface potential of the semiconductor and the charge neutrality in the bulk of the semiconductor. Now we have enough information to solve the Poisson equation. The first step is to fill in for the space charge density and integrating from the surface toward the bulk.

$$\frac{d^2\Psi_P}{dx^2} = -\frac{q}{\epsilon_S}(n_{p0} - p_{p0} + p_p - n_p) = -\frac{q}{\epsilon_S}\{p_{p0}[e^{-\beta\Psi_P} - 1] - n_{p0}[e^{\beta\Psi_P} - 1]\} \quad (\text{Error! Style not defined..9})$$

$$\int_0^{d\Psi_P/dx} \left(\frac{d\Psi_P}{dx}\right) d\left(\frac{d\Psi_P}{dx}\right) = -\frac{q}{\epsilon_S} \int_0^{\Psi_P} \{p_{p0}[e^{-\beta\Psi_P} - 1] - n_{p0}[e^{\beta\Psi_P} - 1]\} d\Psi_P \quad (\text{Error! Style not defined..10})$$

By doing this we implicitly made use of the boundary conditions. The left hand side can be simplified by taking a look at the electric field which is

$$\mathcal{E} = -\frac{d\Psi_P}{dx} \quad (\text{Error! Style not defined..11})$$

Integrating the right hand side leads to the relation between the electric field and the potential

$$\mathcal{E}^2 = \left(\frac{2kT}{q}\right)^2 \left(\frac{qp_{p0}\beta}{2\varepsilon_S}\right) \left\{ [e^{-\beta\Psi_P} + \beta\Psi_P - 1] + \frac{n_{p0}}{p_{p0}} [e^{\beta\Psi_P} - \beta\Psi_P - 1] \right\}. \quad (\text{Error! Style not defined..12})$$

This equation is not user-friendly to handle which is the reason why the following short form is introduced

$$\mathcal{E}(x) = \pm \frac{\sqrt{2}kT}{qL_D} F\left(\beta\Psi_P, \frac{n_{p0}}{p_{p0}}\right). \quad (\text{Error! Style not defined..13})$$

The positive sign is used for  $\Psi_p > 0$  and the negative sign for  $\Psi_p < 0$  because the function F is defined to be always positive. The following two abbreviations were used:

$$L_D = \sqrt{\frac{kT\varepsilon_S}{p_{p0}q^2}} = \sqrt{\frac{\varepsilon_S}{qp_{p0}\beta}} \quad (\text{Error! Style not defined..14})$$

$$F\left(\beta\Psi_P, \frac{n_{p0}}{p_{p0}}\right) = \sqrt{[e^{-\beta\Psi_P} + \beta\Psi_P - 1] + \frac{n_{p0}}{p_{p0}} [e^{\beta\Psi_P} - \beta\Psi_P - 1]} \quad (\text{Error! Style not defined..15})$$

$L_D$  is called the Debye length. Above we could see that the carrier concentration follows an exponential function. The Debye length is the characteristic length at which the carrier concentration dropped by the factor of  $1/e$ .  $e$  is Euler's number.

What we are interested in is the space charge density right at the insulator semiconductor interface ( $\Psi_p = \Psi_s$ ).

$$\mathcal{E}_S = \pm \frac{\sqrt{2}kT}{qL_D} F\left(\beta\Psi_S, \frac{n_{p0}}{p_{p0}}\right) \quad (\text{Error! Style not defined..16})$$

This leads to

$$Q_S = -\varepsilon_S \mathcal{E}_S = \mp \frac{\sqrt{2}\varepsilon_S kT}{qL_D} F\left(\beta\Psi_S, \frac{n_{p0}}{p_{p0}}\right) \quad (\text{Error! Style not defined..17})$$

Please note that the above derivation is valid for all four states (accumulation, depletion, weak and strong inversion).

A typical function of the absolute value of the space charge density in a p type semiconductor in dependency of the surface potential is shown in Figure 2.7.

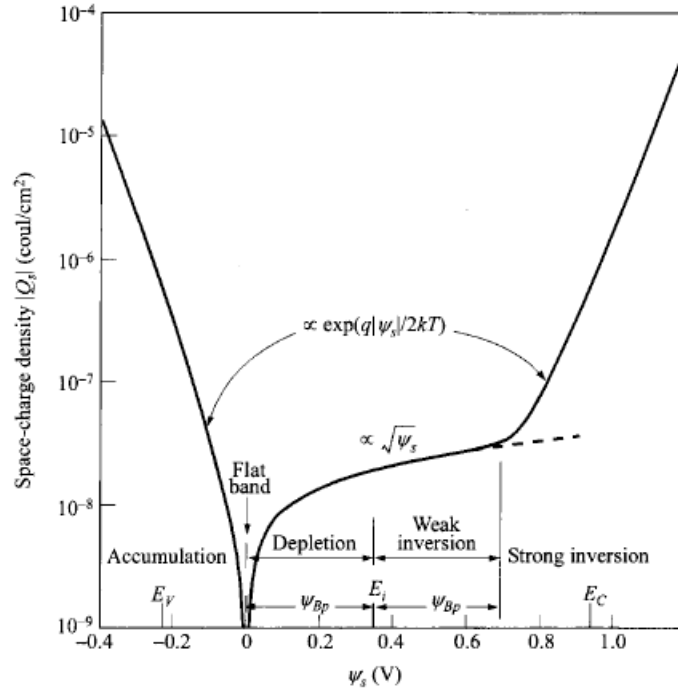


Figure 2.7: Absolute values of the semiconductors space-charge density in dependency of the surface potential for a p-type silicon with  $N_A = 4 \cdot 10^{15} \text{cm}^{-3}$  at room temperature. Image taken from [1].

In this picture all states and all special conditions can be seen. For negative values of the surface potential, which in this semiconductor means accumulation,  $Q_s$  is positive. Hence the function  $F$  is dominated by the first term,  $Q_s$  is proportional to  $e^{\beta|\Psi_s|/2}$ . The flat band condition is fulfilled at  $\Psi_s=0$  at which  $Q_s$  is also zero. At depletion and also in the following states,  $Q_s$  is negative. In the depletion and weak inversion states  $F$  is dominated by the second term which means  $Q_s$  is proportional to  $\sqrt{\Psi_s}$ . The fourth term of  $F$  is dominant in the strong inversion state. This makes  $Q_s$  follow an exponential curve  $e^{\beta|\Psi_s|/2}$ . The borderline between weak and strong inversion is approximately at

$$\Psi_s(\text{strong inversion}) \approx 2\Psi_{Bp} \approx \frac{2kT}{q} \ln\left(\frac{N_A}{n_i}\right) \quad \text{(Error! Style not defined..18)}$$

The bottom line is that one obtains a voltage dependent space charge density. In the accumulation and strong inversion, there is a huge cloud of charge carriers near the insulator semiconductor interface. In between, the charge carriers are pushed away from the insulator semiconductor interface. This leads to a space charge region which again can be seen as a capacitor. It is called the depletion zone capacitor  $C_D$  (Figure 2.8).

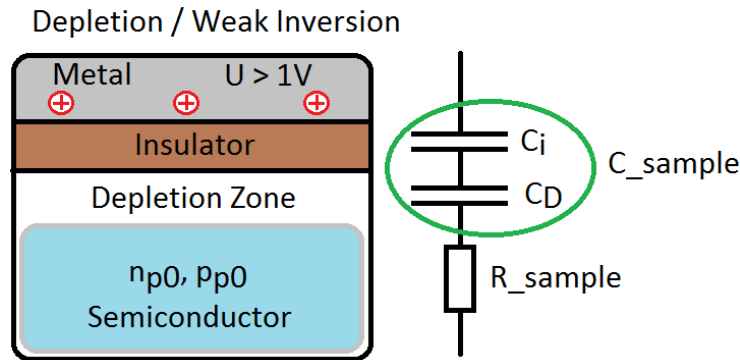


Figure 2.8: Schematic drawing of the MIS structure with a p type semiconductor including a lumped element model for the depletion and weak inversion state.

The total capacity of this structure is

$$C = \frac{C_i C_D}{C_i + C_D} \quad (\text{Error! Style not defined..19})$$

The capacitance  $C_D$  per unit area is simply the derivative of the space charge density  $Q_s$  with respect to the surface potential  $\Psi_s$ .

$$C_D = \frac{dQ_s}{d\Psi_s} = \frac{\epsilon_s}{\sqrt{2}L_D} \frac{1 - e^{-\beta\Psi_s} + \frac{n_{p0}}{p_{p0}} [e^{\beta\Psi_s} - 1]}{F\left(\beta\Psi_s, \frac{n_{p0}}{p_{p0}}\right)} \quad (\text{Error! Style not defined..20})$$

In the equivalent circuit the insulator capacitor  $C_i$  is in series with the depletion zone capacitor  $C_D$ .

The applied voltage  $U$  splits up to the voltage drop in the insulator and the surface potential.

$$U = U_i + \Psi_s \quad (\text{Error! Style not defined..21})$$

The voltage drop in the insulator is proportional to the absolute value of the space charge density  $Q_s$

$$U_i = \frac{|Q_s|d}{\epsilon_i} = \frac{|Q_s|}{C_i} \quad (\text{Error! Style not defined..22})$$

Now we have four unknown variables and four equations. The unknown variables are  $C_D$ ,  $Q_s$ ,  $\Psi_s$ , and  $F$  with the corresponding equations (Error! Style not defined..17), (Error! Style not defined..20), (Error! Style not defined..21) and (Error! Style not defined..22).

A solution in Matlab takes its time and delivers sometimes unstable results if the algorithm, for example the Newton algorithm, does not converge. Since we already know the expected values of the total capacitance  $C$  for high positive and high negative voltages, the area we are interested in is the area at low voltages and therefore low values of the space charge density  $Q_s$ . According to formula (Error! Style not defined..22) low values of  $Q_s$  lead to a low voltage drop  $U_i$  across the insulator, which we will neglect from now on. The applied voltage  $U$ , if it is small, is also the surface potential of the semiconductor  $U = \Psi_s$ .

Everything we need to do is fill in the values of the applied voltage in the formula for the depletion zone capacitance and we can easily calculate the total capacitance of the whole metal-insulator-semiconductor structure.

A typical function of the total capacitance per unit area divided by  $C_i$  can be seen in Figure 2.9

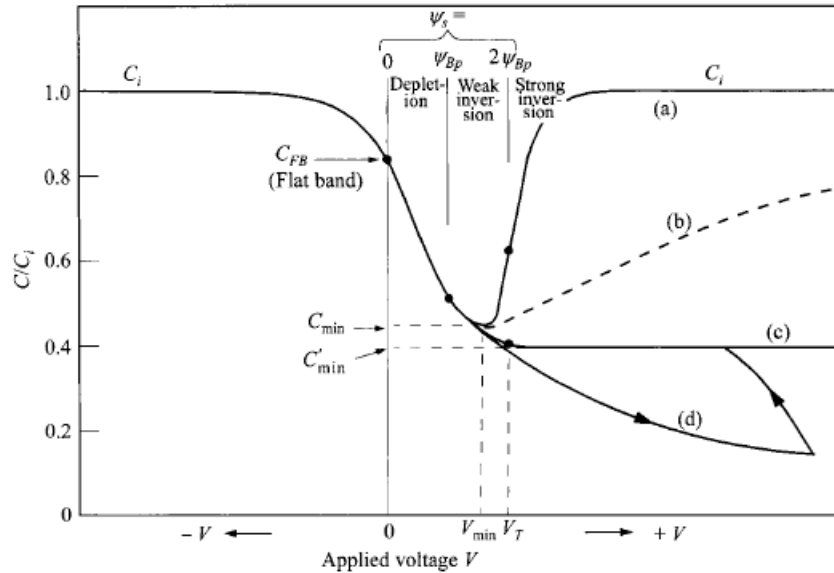


Figure 2.9: Capacitance-voltage curves for a p-type MIS structure low frequencies (a), intermediate frequencies (b), high frequencies (c) and for high frequencies with fast sweep (deep depletion) (d). Image taken from [1].

This graph is true for p-type semiconductors. If you reverse the voltage it becomes valid for n-type semiconductors. The curve which was calculated right now is (a). Strictly seen it is only valid for relatively low frequencies of the applied voltage. At high frequencies the minority charges cannot follow the applied voltage anymore due to the low drift velocity and the low amount of minorities in the semiconductor. As a result the strong inversion state disappears. The capacitance stays at a low level like in curve (c). Curve (b) shows a CV curve for an intermediate frequency and curve (d) is not of interest for this work.

In the high frequency case the minimum capacitance value per unit area  $C'_{min}$  is

$$C'_{min} = \frac{\epsilon_i \epsilon_S}{\epsilon_S d + \epsilon_i W_{Dm}} \quad (\text{Error! Style not defined..23})$$

with the maximum depletion width

$$W_{Dm} \approx \sqrt{\frac{2\epsilon_S \Psi_S(\text{strong inversion})}{q N_A}} \approx \sqrt{\frac{4\epsilon_S kT \ln(N_A/n_i)}{q^2 N_A}} \quad (\text{Error! Style not defined..24})$$

Since the measurements are made between 1 and 20GHz the high frequency case is valid. The conclusion is that we are able to calculate the CV curve for an arbitrary metal-insulator-semiconductor structure for low and high frequencies.

### 2.1.2 Handling of the tip- and gold pad structure

In Figure 2.2 the tip and the underlying probe were simplified as a metal insulator semiconductor structure. To take the tips geometry into account, one can simplify the tip surface as a number of steps according to the Figure 2.10.

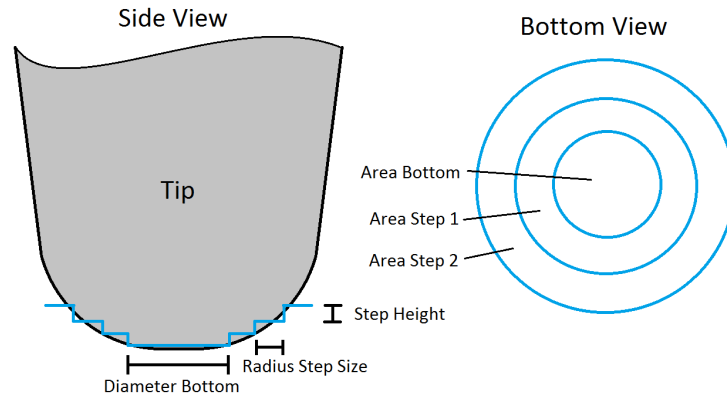


Figure 2.10: Schematic drawing of the tip structure handling.

From every step the area and further the capacitance to the sample can be calculated and switched together according to Figure 2.11.

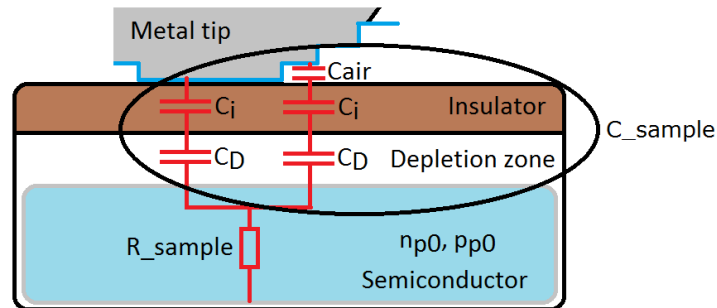


Figure 2.11: Schematic drawing of the capacitances of the tip/insulator/semiconductor structure.

In one line, the three capacitors  $C_{air}$ ,  $C_i$  and  $C_D$  are in series.

$$C_{line} = \frac{1}{1/C_{air} + 1/C_i + 1/C_D} \quad (\text{Error! Style not defined..25})$$

This means the total capacitance of one line is lower than the smallest capacitor value. So, it is senseless to calculate a huge number of steps because then  $C_{air}$  and the total capacitance of the line are very low, and their contribution to the total capacitance of the system is insignificant.

Several samples in the lab consist of a gold metal contact on top of an insulating oxide layer on top of doped silicon (Figure 2.1). Samples of this structure can easily be handled by the model by inserting the

diameter of the gold metal contact into the variable 'Diameter Bottom' in Figure 2.10 and skipping all other lines which are used to model the round curvature of the tip.

### 2.1.3 Analysis

This physical model allows a quantitative analysis of the dependency of the  $C(V)$  curve on certain parameters. Looking at the  $C(V)$  curves capacitance difference between the left and the right side, there are some parameters which increase this capacitance difference when they are increased:

- Diameter of the bottom contact
- Dielectric constant of the oxide layer
- Cone angle of the tip (a little bit)

On the other hand there are some parameters which decrease the  $C(V)$  curves capacitance difference when they are increased:

- Doping concentration of the semiconductor
- Oxide thickness

## 2.2 RLC model

A coaxial cable with an open end can be modelled as an R-L-C resonant circuit [3] where the lumped elements are switched in parallel (Figure 2.12). The open end condition is practically always fulfilled due to the small capacitance of the cantilever/tip/sample system. The R-L-C resonant circuit matches the input impedance of an open end coaxial cable resonator. The capacitance of the cantilever is implicit included in the resonator capacitance  $C$ .

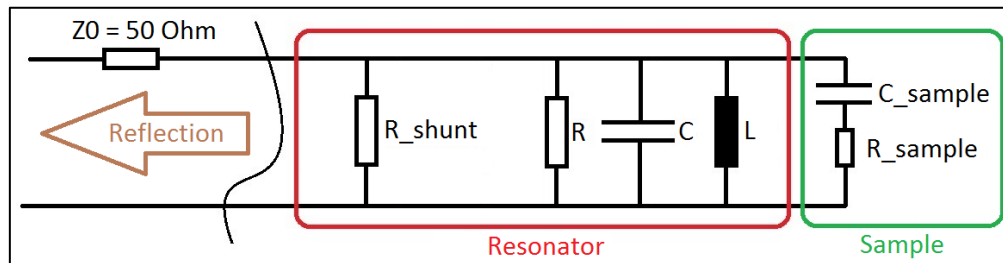


Figure 2.12: Structure of the RLC model containing the resonator equivalent circuit and the sample part.

$Z_0$  symbolises the small coaxial cable. 'R\_shunt' is the  $50\Omega$  shunt resistor. The variable 'C\_sample' stands for a series circuit of the oxide capacitance  $C_i$  and the depletion zone capacitance  $C_D$  of the semiconductor. The variable 'R\_sample' stands for the resistance of the doped silicon.

One can find the right values for the lumped elements by fitting the calculated frequency sweep from the model to those from the measurements. Due to the fact that the sweep should be performed when the tip is in touch with the sample e.g. the gold pad, they play a role when measuring the frequency sweep. Thus, 'C\_sample' and 'R\_sample' were set to certain valid values before finding out the right values for the R-L-C parallel resonant circuit.

In order to produce comparable results, a certain fitting technique was invented to adapt the sweeps to each other which gets rid of the drift problem of the SMM. This technique was also used for the following transmission line model which will be explained in the next chapter. First, 'C\_sample' was set to the capacitance obtained at the accumulation state, which is just the insulator capacitance  $C_i$ . A finite element simulation by Georg Gramse (not yet published) leads to the 'R\_sample' values for the different gold pads on the lowest oxide step according to Table 2.2. Then, an offset was added to the measured sweep in a way that the measured sweep at the measurement frequency and the mean value of the S11(V) curve on the accumulation side are equal. This has the very big advantage that the drift of the SMM has no effect and on the accumulation side of the C(V) curve the correct value appears. This makes the C(V) curves measured at different frequencies comparable. As a further effect one can concentrate on the C(V) curves capacitance difference between the left and the right side of the C(V) curve. By fitting the frequency sweeps' amplitude curve of the RLC model to those of the SMM measured by the PNA, one can find the correct values for the lumped elements. For this purpose, a fitting program was invented which automatically fits the frequency sweep of the RLC model to the frequency sweep of the measurement (Figure 2.13). The vertical black lines lie at the border of the area where the fitting program tries to minimize the difference between the two curves. The vertical green line lies at the frequency where measurements were made.

**Table 2.2: Gold pad diameter values with the proper 'R\_sample' values.**

<b>gold pad diameter [<math>\mu\text{m}</math>]</b>	<b>R_sample [<math>\Omega</math>]</b>
3.5	110
2.5	40
1.7	31
0.7	10

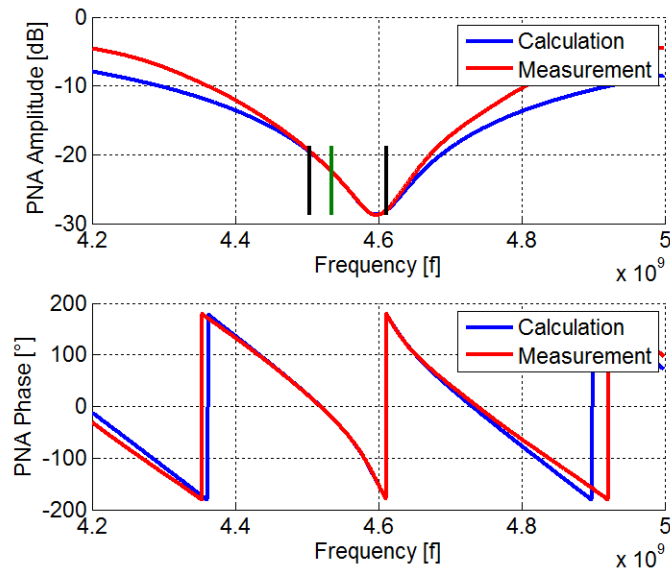


Figure 2.13: Frequency sweep of the measurements at about 4.6GHz (red) and the fitted frequency sweep of the RLC model (blue).

Assuming an open end coaxial cable at which we apply a voltage with a continuously increasing frequency, one can imagine that the phase of the reflected signal is continuously falling. The only exception is when there are two coaxial cables in series. Then the phase can be rising near the resonance peaks. But the phase of the pure RLC model can only be +/- 90° with a more or less smooth transition in between. To match the phase of the model to the measured frequency sweep, a phase matching formula was applied.

$$\varphi_{model} = \varphi_{RLC} + c_{linear\_correction} \cdot f + c_{offset}$$

(Error! Style not defined..26)

By fitting the phase of the model to the measured phase one can find the correct values for  $c_{linear\_correction}$  and  $c_{offset}$ . The transition close to the resonance is covered by the R-L-C circuit in almost every case, but sometimes the phase of the model  $\varphi_{RLC}$  was inverted to match rising and falling phase transitions near the resonance (Figure 2.14).

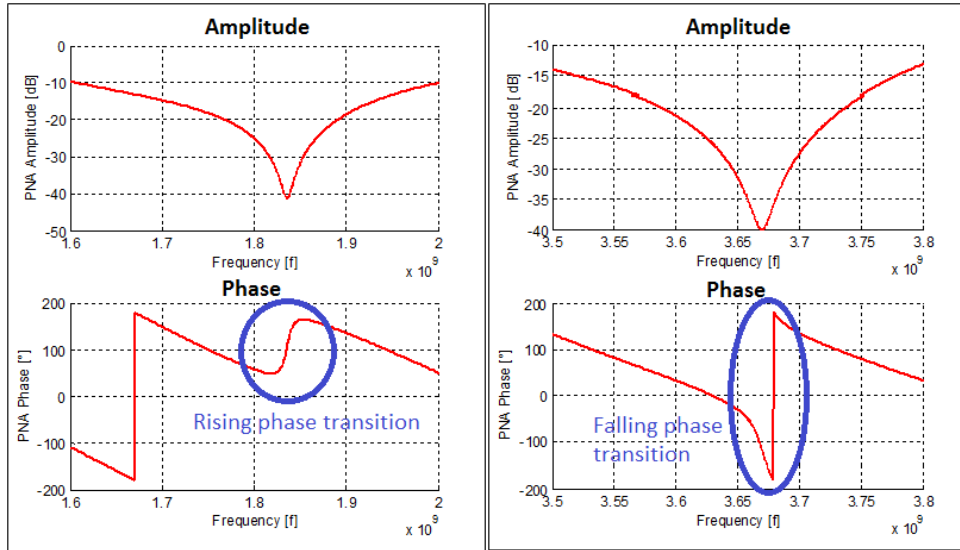


Figure 2.14: Rising and falling phase transition at the resonance frequency.

Once fitted, this model allows the conversion of measured S11 data into capacitance values from the sample, and the conversion from theoretical capacitance values from a sample into theoretical S11 values. The first application is more of interest.

### 2.3 Transmission line model

To understand the working principle and to see the advantages and disadvantages of the RLC model, a transmission line model was invented. The model which was implemented in MATLAB is shown in Figure 2.15.

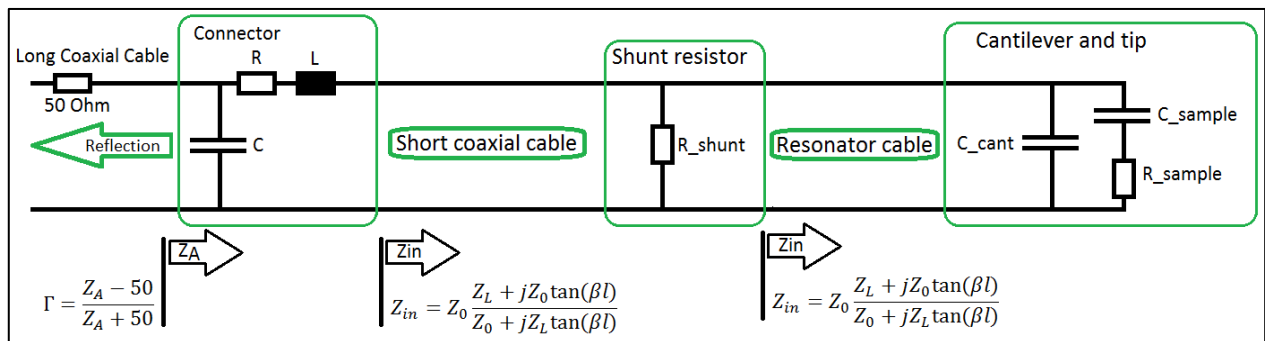
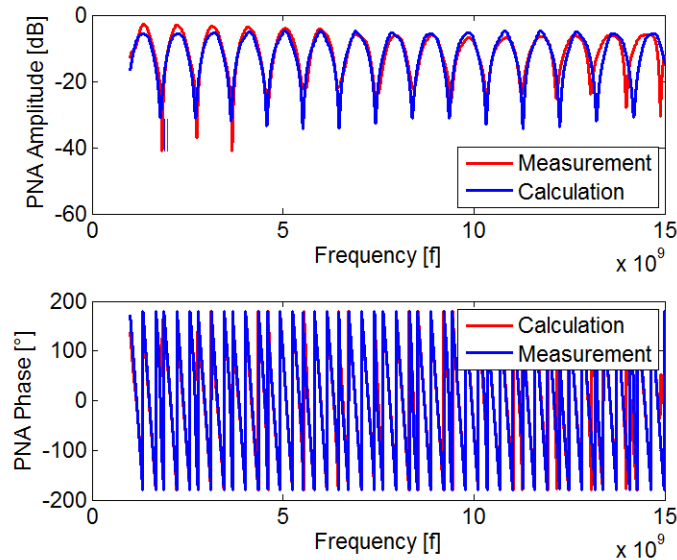


Figure 2.15: Structure of the transmission line model.

With the formula

$$Z_{in} = Z_0 \frac{Z_L + jZ_0 \tan(\beta l)}{Z_0 + jZ_L \tan(\beta l)} \quad (\text{Error! Style not defined..27})$$

one can calculate the input impedance of a cable when terminated with the load impedance  $Z_L$ .  $\beta$  is the wavenumber and  $l$  is the length of the cable. There are 8 unknown variables in this equivalent circuit which are the cantilever capacitance 'C\_cant', the impedance  $Z_0$  and the wavenumber length product  $\beta l$  of the two coaxial cables and the resistance, capacitance and impedance of the connector. The application is similar to the RLC model. By fitting the resonance curve of the transmission line model to those of the SMM measured by the PNA (Figure 2.17), one can find the correct values for the lumped elements in the model. A fit for the frequency range between 1GHz and 15GHz is shown in Figure 2.16.



**Figure 2.16: Result of a fitting procedure in the frequency range between 1GHz and 15GHz with the transmission line model. The upper window shows the PNA amplitude and the lower window shows the PNA phase.**

If only one resonance minima should be fitted, one can set the impedance and the resistance of the connector to zero to avoid an over-determination of the system. The result of a fitting procedure of a single resonance minimum is shown in Figure 2.17.

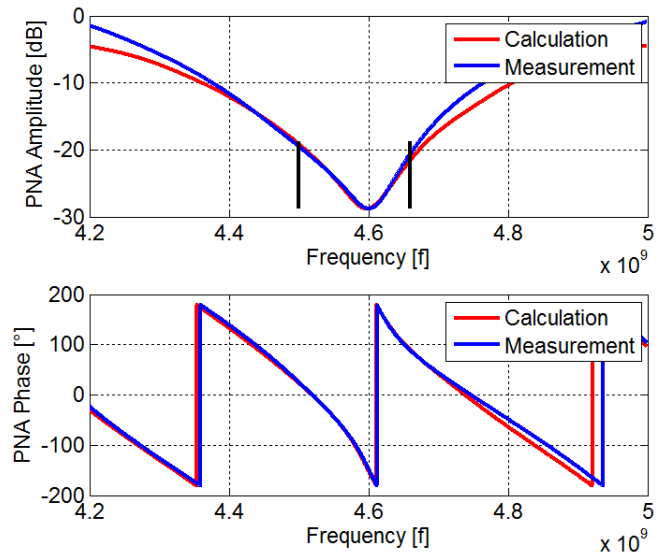


Figure 2.17: Frequency sweep of the measurements at about 4.6GHz (red) and the fitted frequency sweep of the transmission line model (blue).

The vertical black lines in Figure 2.17 lie at the borders within the automatic fitting algorithm tries to minimize the difference between the measured frequency sweep and the frequency sweep of the transmission line model.

## 2.4 Model analysis and comparison

The interesting thing now is whether the models show a similar response to a change in capacitance or not. This can be tested by choosing a resonance minima, fitting the lumped elements of the models, changing the 'C\_sample' variable and observe the reaction of the S11(C) parameter when the measurement frequency stays constant. This was done for many different resonance minima. The results are shown in Figure 2.18. The variable 'R\_Sample' was chosen to be uniformly zero. A non-zero value of 'R\_Sample' would lead to a stronger bending of the curve.

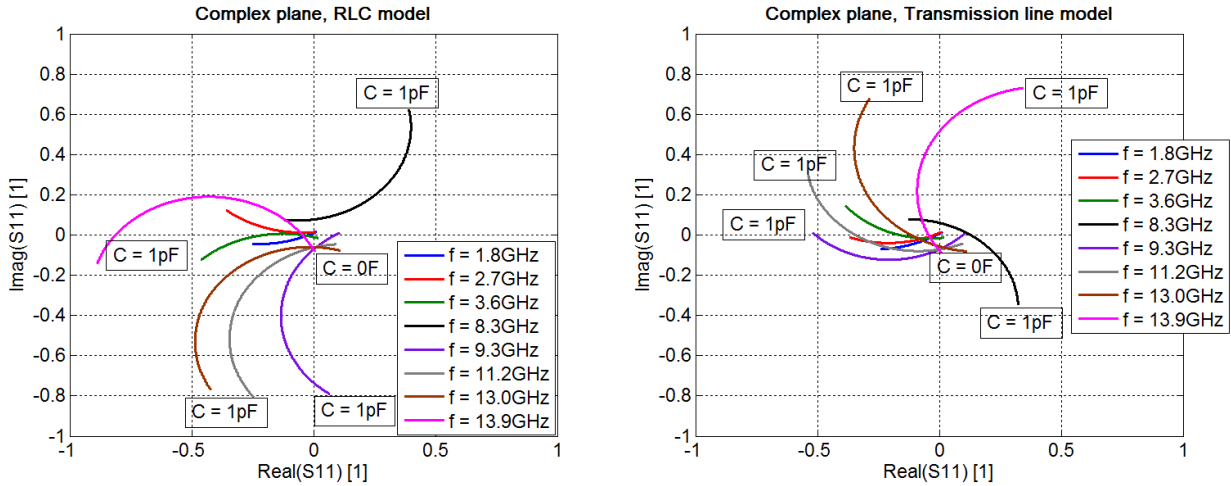


Figure 2.18: Complex plane with the S11 parameter according to the RLC model (left) and the transmission line model (right), when the variable 'C\_Sample' is varied between 0 and 1pF.

Some measurement frequencies (1.8GHz and 2.7GHz in the RLC model results) lead to a bending in clockwise direction and some in counter clockwise direction. Taking a detailed look at both images, one can recognize that every curve (except the curves at 8.3GHz and 13.9GHz) tend to the left direction for low capacitance values. This means that for most measurement frequencies, a small increasing capacitance value means a S11 value shifting to the left, according to the models. Thus, for the measurements, we expect S11 values tending to the left.

Also, both models show that, the smaller the measurement frequency is, the smaller is the S11(C) curve which can be interpreted as a smaller sensitivity to capacitance changes at lower frequencies. Table 2.3 shows the length of the S11(C) curve when varying the sample capacitance between 0 and 1pF for different measurement frequencies. Thus, for the measurements, we expect a bigger change in S11 value at higher frequencies.

Table 2.3: Length of the S11(C) curve on the complex plane between 0 and 1pF according to the RLC model and the transmission line model.

Frequency	Length of the S11(C) curve on the complex plane between 0 and 1pF	
	RLC model	Transmission line model
1.8	0.2600	0.26
2.7	0.37	0.37
3.6	0.48	0.40
8.3	0.72	0.50
9.3	0.79	0.50
11.2	0.83	0.58
13.0	0.89	0.77
13.9	0.91	0.82

Figure 2.18 reveals some differences between the two models. The direct comparison in Figure 2.19 makes it clearer.

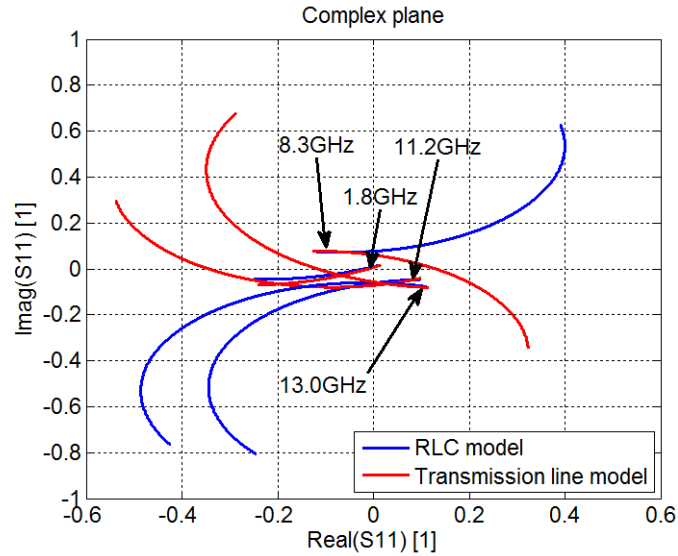


Figure 2.19: Comparison of the S11 parameter according to the RLC model and the transmission line model in the complex plane when the variable 'C\_Sample' is varied between 0 and 1pF.

One can see that the models are similar at low capacitance values. Hence the value of 'C\_Sample' at the curve fitting process was also low, it is more correct to say the models are similar for low capacitance changes. The capacitance value of 1pF is enormous for SMM standards. It was only chosen to be so big so one could see the curvature better. The bottom line of this is that for normal applications like S11(V) curves where the capacitance change is way below 1pF, we expect that the two models deliver similar capacitance values.

### 3 SMM Measurements and analysis

After the theoretical background is done one of the first steps was to level up the quality of the measurements to ensure reproducible  $S_{11}(V)$  curves. After that, the models and the Black-Box calibration method were used to convert the measured  $S_{11}$  values into capacitance values and analyse them.

#### 3.1 SMM Measurements

Before starting the measurements, the best sample for evaluating the validity of the models had to be found.

##### 3.1.1 MC2 sample

The sample called 'MC2' (Figure 3.1) [4] was chosen to be the testing sample.

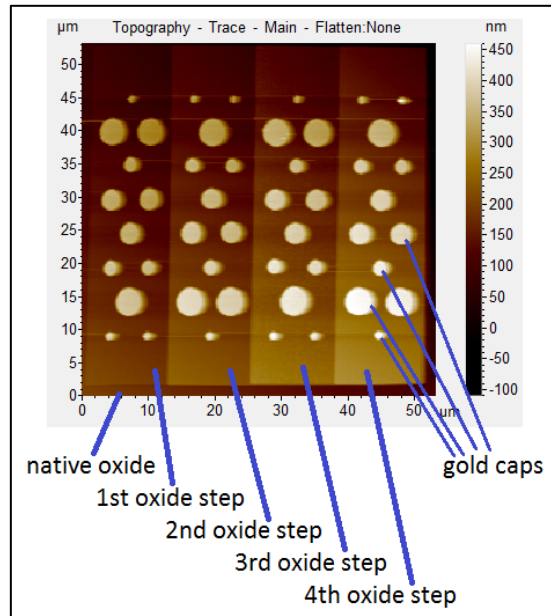


Figure 3.1: Topographic image of the MC2 sample.

This sample provides four different gold diameter sizes on silicon dioxide with four different thicknesses. Beyond this lies n-doped silicon with a doping concentration of about  $10^{17}$   $1/\text{cm}^3$ . One obtains measurable  $C(V)$  curves only on the first oxide step with an oxide thickness of about 30nm. The measured capacitance difference on other steps (approximately 100, 150 and 200nm thick) is beyond the noise level. So, the models can be tested on four different capacitor diameters ( $3.5\mu\text{m}$ ,  $2.5\mu\text{m}$ ,  $1.7\mu\text{m}$  and  $0.7\mu\text{m}$ ) on a 30nm thick oxide on top of n-doped silicon.

A good tip for measuring on the gold caps is to use cantilevers with a thin tip diameter. This increases the quality of the electric contact between the tip and the gold pad. This behaviour can be understood when

taking the thin water film due to the humidity of the air into account. A thin tip can puncture the surface tension of the water film easier and reach the gold surface.

### 3.1.2 Image measurements and conversion theory

The first thing to do is to make a quick overview scan of the sample to make sure all structures are within the scan area (Figure 3.2). After this, the tip was placed on an area where the electric properties are known. The biggest capacitor on the sample with a gold pad diameter of  $3.5\mu\text{m}$  and an oxide height of  $30\text{nm}$  was chosen for every image in this work. On this certain area the frequency sweep was performed and a measurement frequency was chosen. The associated capacitance and resistance according to the simulation results of Georg Gramse, which aren't published yet, are inserted as values for 'C\_sample' and 'R\_sample' of the RLC model and the transmission line model. The other variables of the models were found by fitting the sweeps to each other. Now that the models are complete one can apply them on the images which were scanned at this measurement frequency. This procedure delivers 'C\_sample' and 'R\_sample' values of the samples according to the models.

A similar procedure is used for the conversion with the Black Box calibration method but there is no sweep needed. On the contra side one has to know the right capacitance and resistance values of three different spot on the sample within the scan area. The rest was explained in chapter 3.

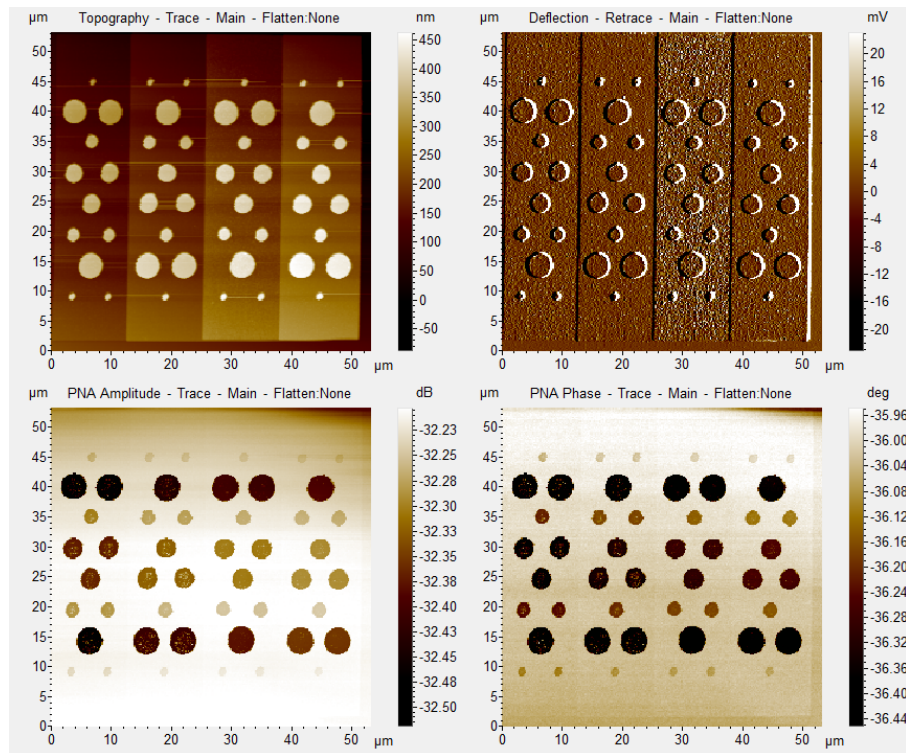


Figure 3.2: Topography (upper left), Deflection (upper right) and PNA signal (amplitude in the lower left window and phase in the lower right window) at 3.6GHz of the MC2 sample. The different oxide steps with the gold pads on top are visible.

### 3.1.3 S11(V) curve measurements

Several methods of measuring S11(V) curves were tested (sawtooth method [2], pointwise C-V technique [2]), but the results were not satisfying. The reliability, the voltage span, the speed and/or the physical correctness of the results weren't sufficient.

Agilent's latest PicoView versions (1.15 and follow-up versions) include a simple, fast and reliable way to measure S11(V) curves without any additional hardware. The proper settings for this measurement tool are now shown.

#### 3.1.3.1 Start-up

To measure capacitance voltage curves with PicoView one can use the Spectroscopy window and choose the expert mode. The next step is to adapt the measurement settings. All S11(V) curves in this work were uniformly measured between -10V and +10V with 500 measurement point within this voltage range. One can measure several curves in one turn and average them to lower the noise level. All curves in this work are the mean value of 5 to 10 measurement curves. After pressing the big blue start button PicoView starts automatically measuring the chosen amount of S11(V) curves which should look similar to Figure 3.3

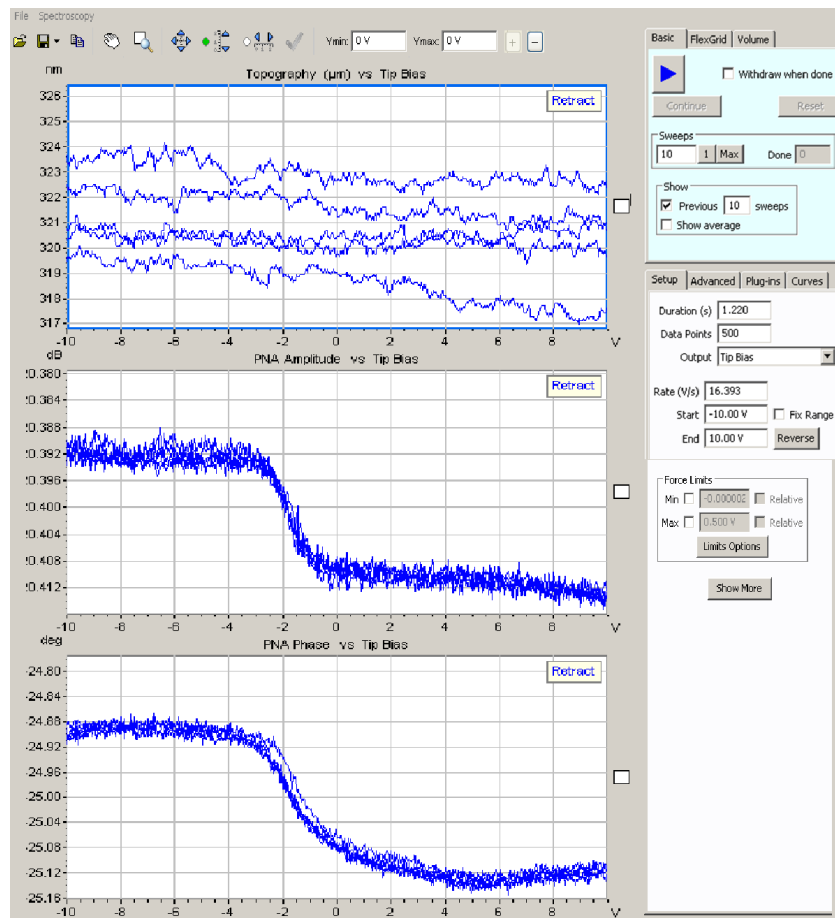


Figure 3.3: Example for measured S11(V) curves.

Measuring and displaying the topography isn't necessary but it is an easy way to test whether the tip is still on top of an upraised structure, for example the gold contact of a MIS structure, or not.

### 3.1.3.2 Electric charging

It is eye-catching that the transition of the curve in Figure 3.3 lies between minus three and zero volt instead of minus one and zero. This can be partly explained by the voltage drop along the 30nm thick oxide, but also a charge-up effect is present. For example if one measures the very first set of curves on a measurement day, the curves look like in Figure 3.4.

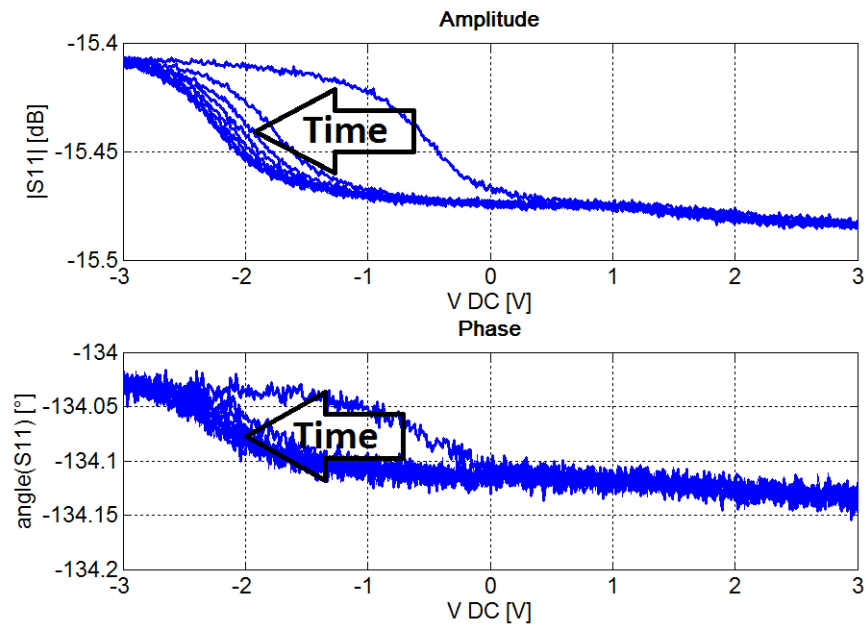


Figure 3.4: S11(V) curves with visible charge up effect.

The very first curve has the maximum slope around -0.5V which goes along with the theory from chapter 3.1. Every following curve is shifted to the left. The shift ends when the maximum slope is about -2V. This speaks for a sort of charging effect which was only obtained at samples with gold caps on it. When measuring simpler semiconductor samples with a native oxide on top, this charging effect wasn't noticeable. The source of this effect isn't yet completely understood, but it can be minimized by keeping the variable 'Rate (V/s)' low. A value of 2V/s turned out to be sufficient. Also, the user should make sure to measure with a negative start voltage and a positive end voltage. Otherwise the charging effects shift the maximum slope of the S11(V) curve to about -7V. It wasn't obtained that this charging effect changes the S11 amplitude and phase in the accumulation or the strong inversion state. It just shifts the curve towards negative voltages. Hence, this effect should not interfere with the C(V) curves capacitance difference information.

### 3.1.3.3 Reliability of the measurements

PicoView allows a lot of system settings to be changed. This subchapter concerns about the reliability of the measurements and the influence of such system settings on the S11(V) curves. Also which settings were used to level up the measurements on a uniform basis will be discussed.

### 3.1.3.3.1 Control of the capacitor size behaviour

As previous measurements and logical thoughts suggest, the difference between the left and the right side of the  $S_{11}(V)$  amplitude and phase curve should increase as the capacitor size increases. More accurate is to take a look at the complex plane where there should be two clouds of measurement points whose distance should increase as the capacitor size increases according to Figure 3.5.

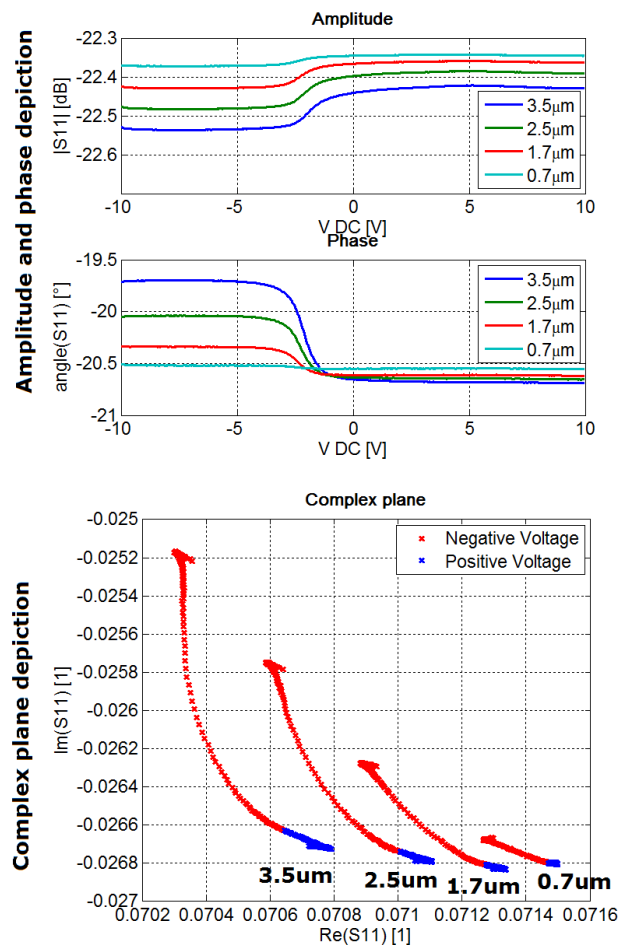


Figure 3.5:  $S_{11}(V)$  curves and the associated complex plane diagram measured on four different gold pad sizes on a 30nm thick oxide at 3.655128GHz. The comparison shows how the straight lines in the  $S_{11}(V)$  graph form the cloud of points in the complex plane.

The distance between the clouds of points is bigger for bigger capacitor sizes, as the complex plane in Figure 3.5 indicates. Figure 3.6 shows a further control measurement at 1.8GHz.

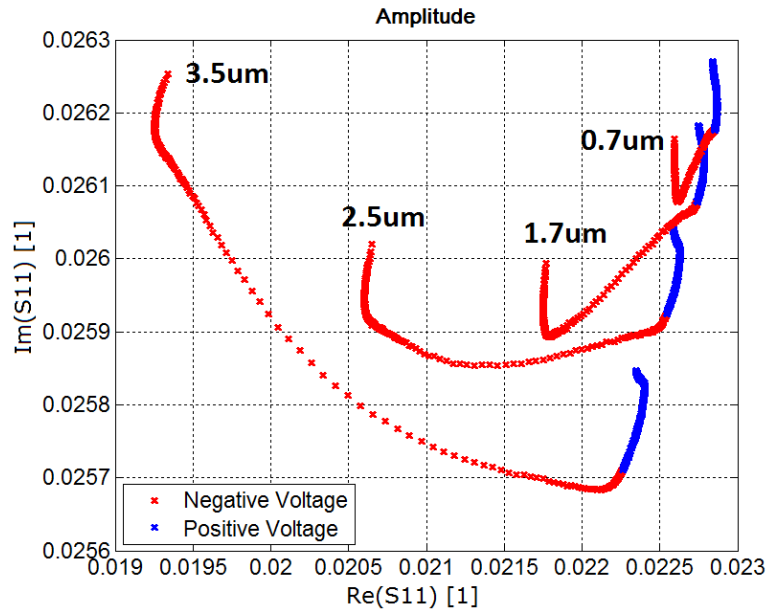


Figure 3.6: Complex plane with the measurements on four different gold pad sizes on a 30nm thick oxide at 1.814744GHz.

Also at 1.8GHz, the clouds of measurement points are farer away from each other for bigger capacitor sizes than for smaller one. This first control measurement went exactly as expected.

### 3.1.3.3.2 Influence of the PNA power

The first setting whose influence was investigated was the PNA power.  $S_{11}(V)$  measurements were made with different PNA signal power at 3.6GHz (Figure 3.7).

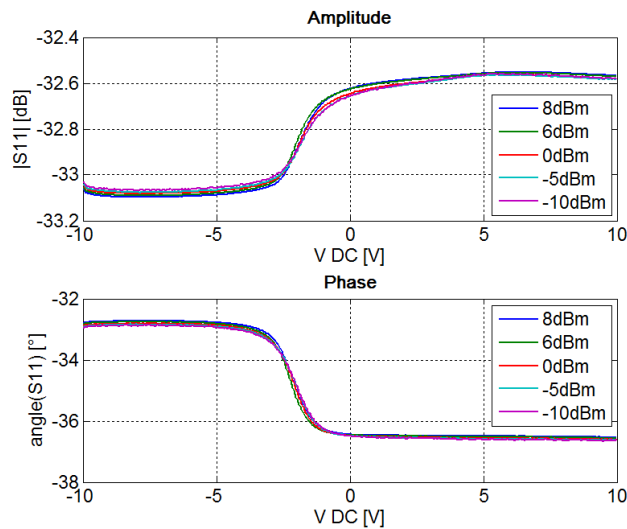


Figure 3.7:  $S_{11}(V)$  curves for different PNA power setting measured on a 3.5um gold pad on a 30nm thick oxide at 3.652564GHz.

On the first sight the curves seem to be equivalent. Due to the drift of the system it becomes easier to norm the curves to be zero at the accumulation side. This gives a better insight into the power dependency of the S11(V) curve difference between the left and the right side.

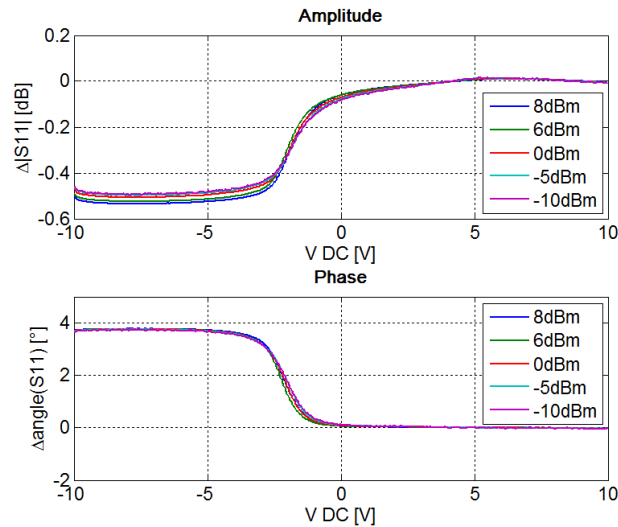


Figure 3.8: S11(V) curves for different PNA power setting measured on a 3.5um gold pad on a 30nm thick oxide at 3.652564GHz. The curves were normed in a way that the values at the accumulation side are zero.

Now one can see that the change of the S11 amplitude slightly decreases with the decrease of PNA power while the change of the S11 phase stays constant. Even more detailed is the calculated difference where the mean value of the curves between -10V and -6V were subtracted from the mean value of the curves between 6V and 10V (Table 3.1). So, the change is positive when the curve rises with increasing voltage and vice versa.

Table 3.1: Difference between the left and the right side of the S11(V) amplitude and phase curve for different PNA power settings measured on a 3.5um gold pad on a 30nm thick oxide at 3.652564GHz.

PNA power [dBm]	Amplitude change [dB]	Phase change [°]
8	0.527	-3.751
6	0.516	-3.741
0	0.498	-3.730
-5	0.489	-3.717
-10	0.484	-3.705

Now, beside the already recognized decrease of the PNA amplitude, one can also recognize a slight influence of the PNA power on the phase curvature. The amplitude difference changes up to 8% and the phase difference changes around 1%. If this has an influence on the resulting capacitance values according to the models will be investigated in chapter 4.2.

The same measurements were made at 1.8GHz. After the standardization at the accumulation side, the curves look like in Figure 3.9.

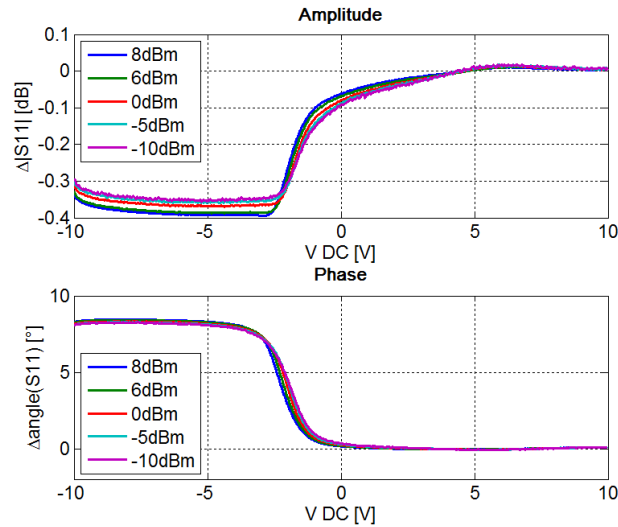


Figure 3.9: S11(V) curves for different PNA power setting measured on a 3.5um gold pad on a 30nm thick oxide at 1.824338GHz. The curves were normed in a way that the values at the accumulation side are zero.

The best insight gives again the calculated changes of the curves in tabular form (Table 3.2).

Table 3.2: Difference between the left and the right side of the S11(V) amplitude and phase curve for different PNA power settings measured on a 3.5um gold pad on a 30nm thick oxide at 1.824338GHz.

PNA power [dBm]	Amplitude change [dB]	Phase change [°]
<b>8</b>	0.372	-8.452
<b>6</b>	0.364	-8.404
<b>0</b>	0.345	-8.315
<b>-5</b>	0.335	-8.260
<b>-10</b>	0.329	-8.230

The amplitude difference changes up to 11% and the phase difference changes around 2.6%. In what way the PNA power influence has an effect on the converted capacitance values will be part of the later chapters. For the further measurements a PNA power of 6dBm was chosen to be the uniform standard for this work.

### 3.1.3.3.3 Influence of the distance between measurement frequency and resonance minimum

Even after choosing the resonance minimum where the measurement should be performed, the exact measurement frequency stays a freedom of choice. The next measurements were made with different measurement frequencies around the resonance minimum at 3.6GHz (Figure 3.10).

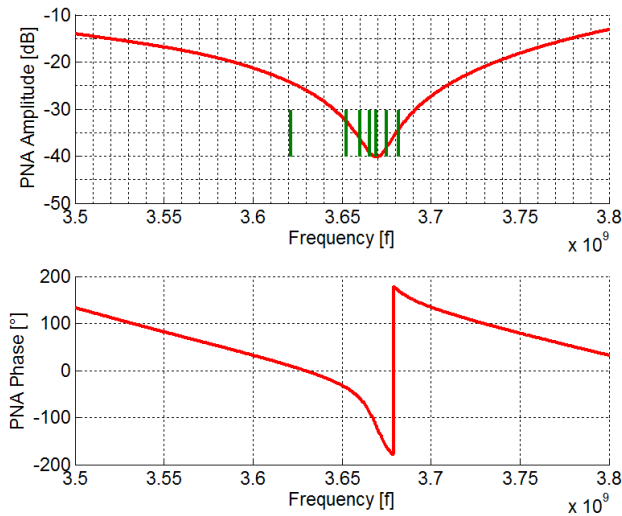


Figure 3.10:  $S_{11}(f)$  frequency sweep around the resonance minimum at 3.66GHz (red). The vertical green lines lie at the measurement frequencies.

The measured and standardized  $S_{11}(V)$  curves at these measurement frequencies are shown in Figure 3.11.

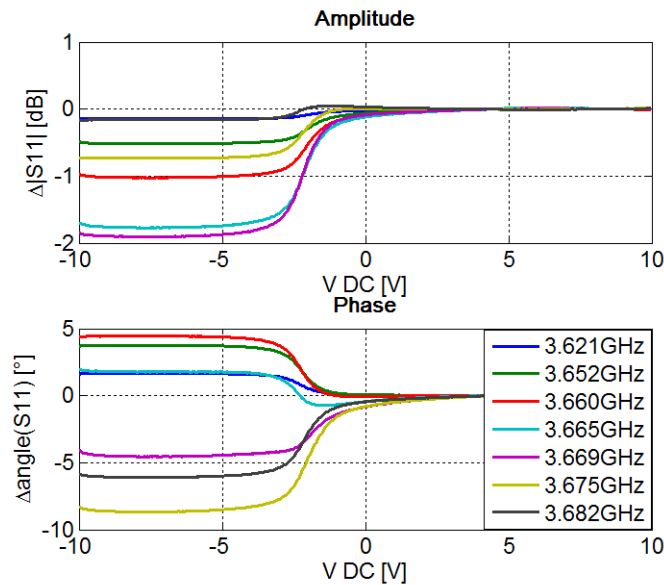


Figure 3.11:  $S_{11}(V)$  curves measured on a 3.5 $\mu$ m gold pad on a 30nm thick oxide with different measurement frequencies around 3.6GHz. The curves were normed in a way that the values at the accumulation side are zero.

The curves reveal that the closer to the measurement frequency lies to the resonance frequency, the bigger is the difference of the  $S_{11}(V)$  amplitude between the left and the right side. The  $S_{11}(V)$  phase curve on the other side shows a completely different behaviour. The phase change is negative on the left side of the resonance minimum, and positive on the right side. The maximum phase change is not at the

centre of the resonance but a little bit shifted. This behaviour can also be seen in Table 3.3 containing the S11 values differences between the left and the right side and in Figure 3.12.

**Table 3.3: Difference between the left and the right side of the S11(V) amplitude and phase curve measured on a 3.5um gold pad on a 30nm thick oxide with different measurement frequencies around 3.6GHz.**

Measurement frequency	Amplitude change [dB]	Phase change [°]
3.621GHz	0,14	-1,64
3.652GHz	0,51	-3,74
3.660GHz	1,01	-4,42
3.665GHz	1,75	-1,79
3.669GHz	1,88	4,46
3.675GHz	0,72	8,56
3.682GHz	0,15	6,03

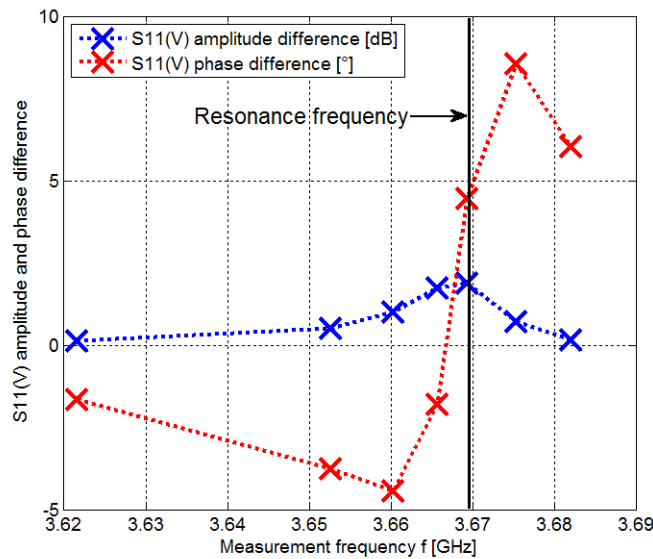


**Figure 3.12: Difference between the left and the right side of the S11(V) amplitude and phase curve measured on a 3.5um gold pad on a 30nm thick oxide plotted over different measurement frequencies around 3.6GHz.**

As a consequence all following measurements were made always on the left side of the resonance minimum. If and how much the exact measurement frequency influences the resulting capacitance values calculated by the two models will be discussed in chapter 4.2.

To have validation similar measurements were made at the resonance minimum at 1.8GHz. Figure 3.13 shows the frequency sweep and the measurement frequencies around 1.8GHz.

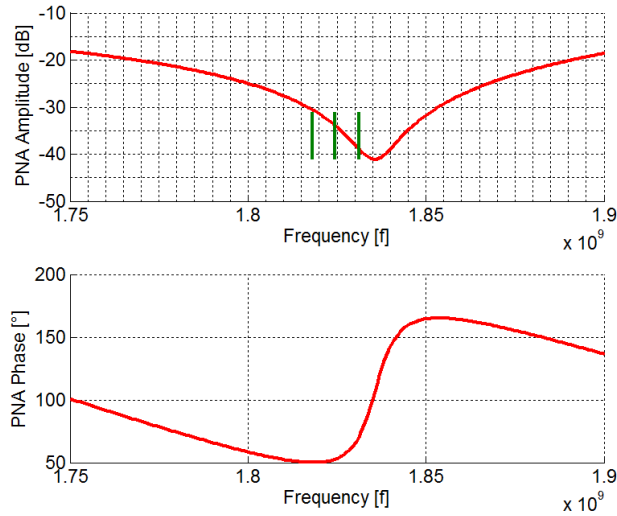


Figure 3.13:  $S_{11}(f)$  frequency sweep around the resonance minimum at 1.8GHz (red). The vertical green lines lie at the measurement frequencies.

The  $S_{11}(V)$  curves which were measured at the three measurement frequencies are plotted in Figure 3.14.

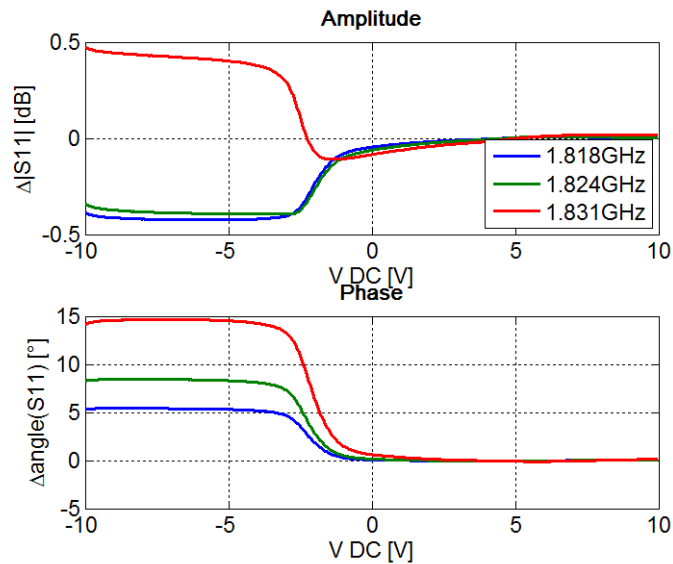


Figure 3.14:  $S_{11}(V)$  curves measured on a 3.5um gold pad on a 30nm thick oxide with different measurement frequencies around 1.8GHz. The curves were normed in a way that the values at the accumulation side are zero.

The  $S_{11}(V)$  curve at 1.83GHz (red) looks different than the others. But by taking a look at the curves in the complex plane they look way more similar (Figure 3.15).

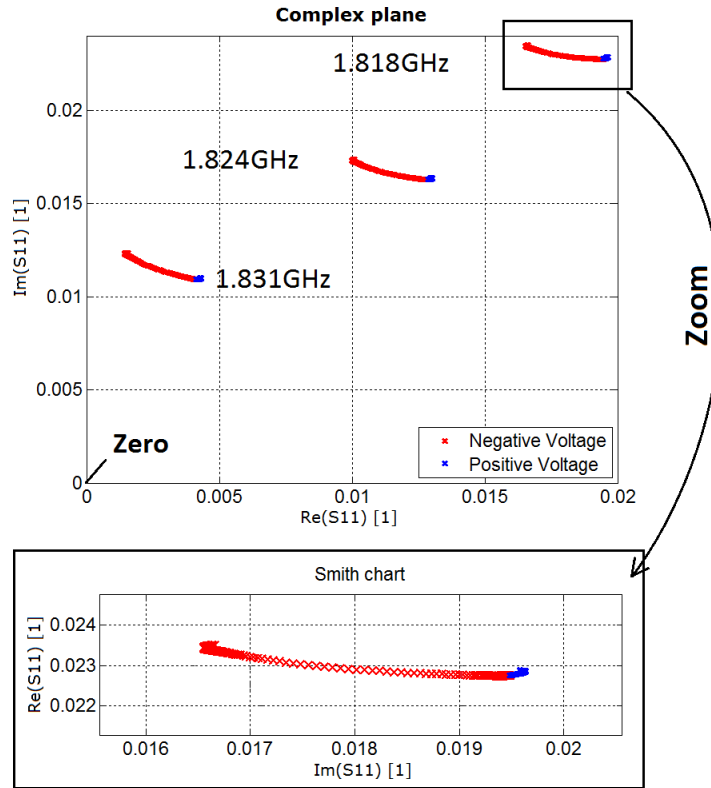


Figure 3.15: Complex plane with the S11(V) curves measured on a 3.5 $\mu$ m gold pad on a 30nm thick oxide with different measurement frequencies around 1.8GHz.

In this diagram, they look way more similar. The S11 amplitude and phase changes can again be displayed over the measurement frequency.

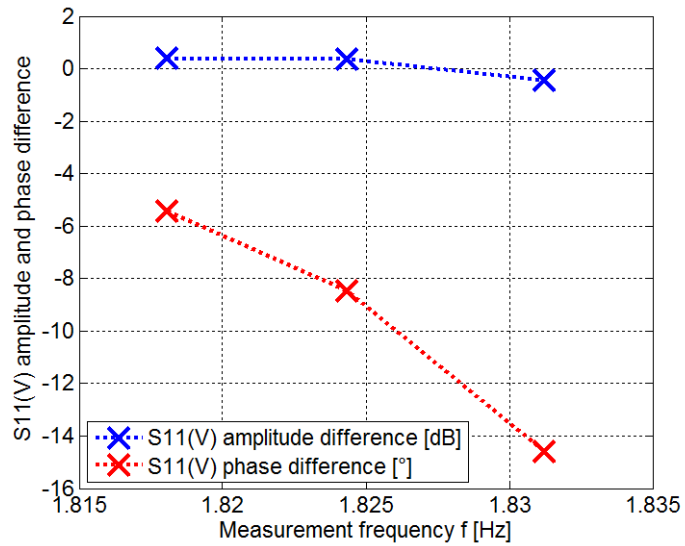


Figure 3.16: Difference between the left and the right side of the S11(V) amplitude and phase curve measured on a 3.5 $\mu$ m gold pad on a 30nm thick oxide plotted over different measurement frequencies around 1.8GHz.

The same behaviour like at 3.6GHz (Figure 3.12 at the left side) is obtained.

The next step was to systematically carry out measurements at many different frequencies for further analysis and comparison with the models.

### 3.1.4 Measurement analysis

The model analysis in chapter 2.4 led to the expectation that the S11 values tend to the left in the complex plane. To proof this expectation, Figure 3.17 shows every S11(V) curve in the complex plane measured on the 3.5 $\mu$ m gold pad at different frequencies. A closed up picture of every curve can be seen at the border of the image.

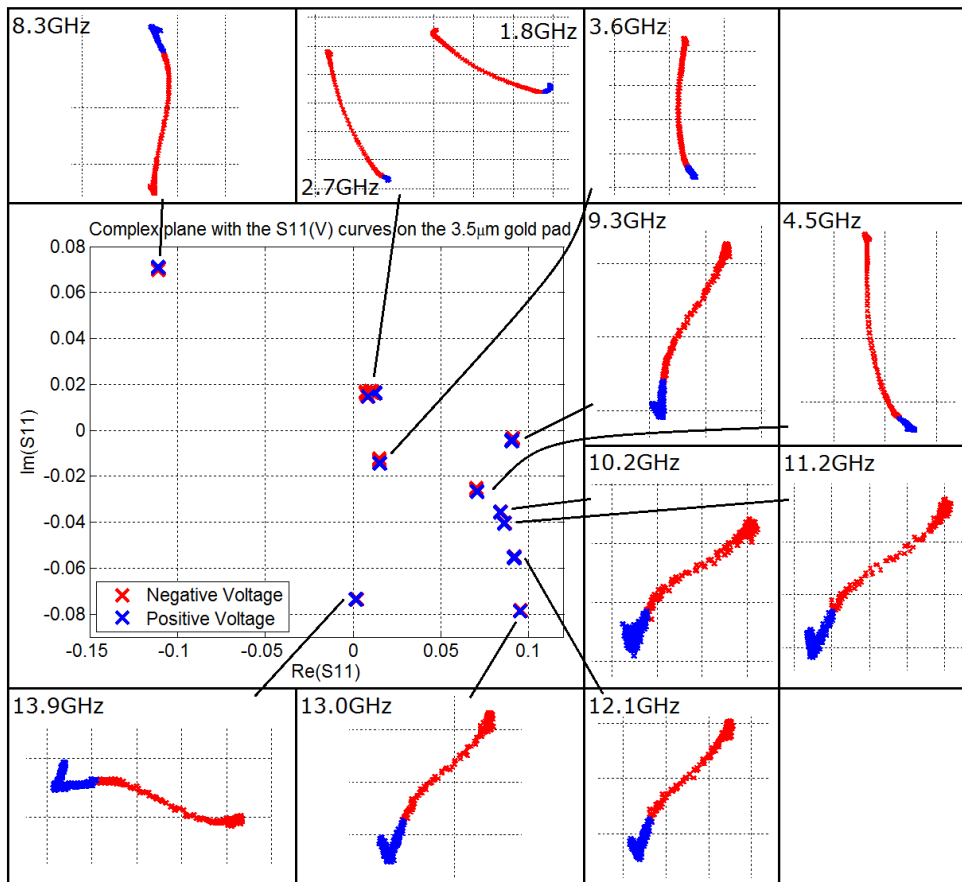


Figure 3.17: Complex plane with all S11(V) curves measured on the 3.5 $\mu$ m gold pad measured with various measurement frequencies. Every S11(V) curve is zoomed out in an extra window.

There is no tendency to the left visible. Figure 3.18 is a graph with the complex S11(V) measurement curves in the complex plane (left image). The arrows show the direction from the S11 values at negative voltages to those at positive voltages as the right image indicates. One can observe that the direction of the S11(V) curves slope tends to circle around the zero point.

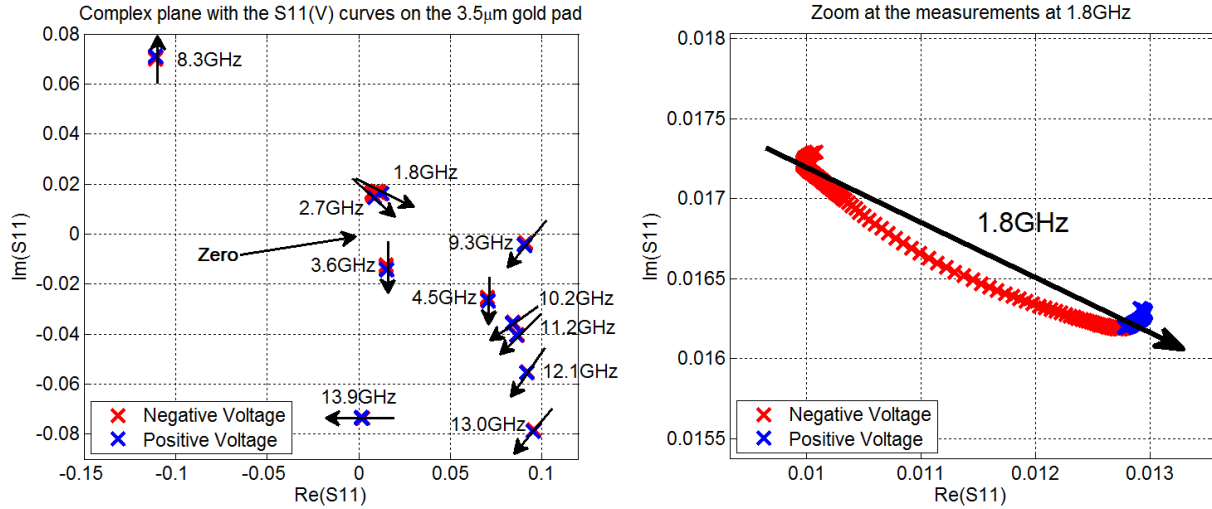


Figure 3.18: Left: Complex plane with all  $S_{11}(V)$  curves measured on the  $3.5\mu\text{m}$  gold pad. The arrows show the direction of the  $S_{11}(V)$  curves from values at negative voltages to the values at positive voltages. Right: Zoom to the measurement at 1.8GHz to show the arrangement of the arrows.

A direct comparison can be seen in Figure 3.19. There, the measurements on the right (a) are pictured together with the results from Figure 2.18 for the RLC model (b) and the transmission line model (c). The only difference to Figure 2.18 is that the value of 'C\_sample' was varied only between 0fF and 10fF. As mentioned in chapter 2.4, the models foresee  $S_{11}$  values tending to the left for nearly every measurement frequency when the sample capacitance is increased.

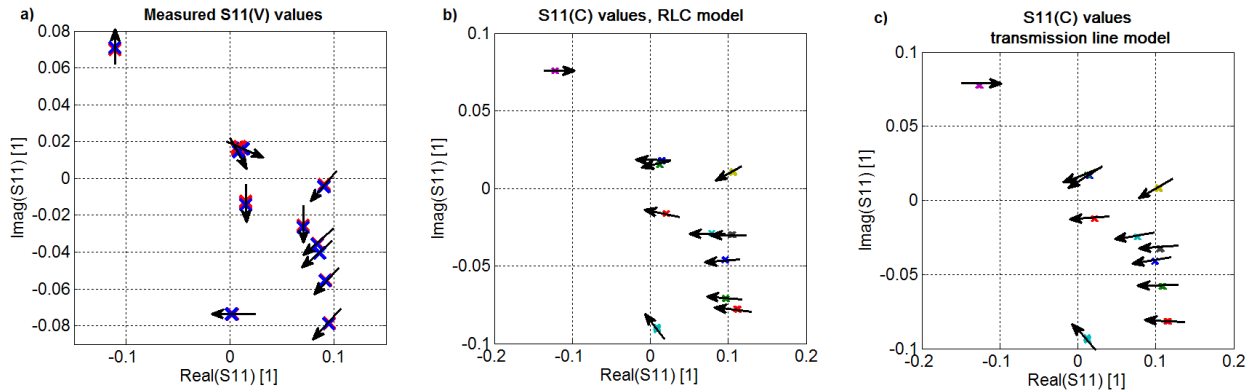


Figure 3.19: Comparison in the complex plane of the direction of the measured  $S_{11}(V)$  curves (a) and the calculated  $S_{11}(C)$  values according to the RLC model (b) and the transmission line model (c).

Here one can see again that there is not a big difference between the RLC model and the transmission line model for little capacitance changes.

## 3.2 Data analysis using SMM models

S11(V) measurements were made at many different frequencies and on 4 different capacitor sizes. In addition several images of the MC2 sample were made which can also be converted with the RLC model, the transmission line model and the Black-Box calibration [6]. The results and the analysis of them will be presented in this chapter.

### 3.2.1 Image conversion results

The first image was made at 3.6GHz. The position where the sweep was measured was always the biggest capacitor with a diameter of  $3.5\mu\text{m}$  on the  $30\text{nm}$  oxide step.

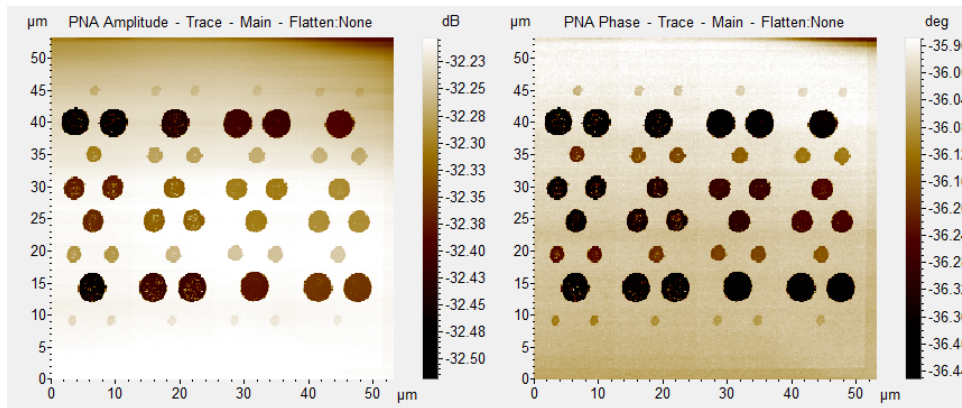


Figure 3.20: PNA amplitude and phase image of the MC2 sample at 3.652564GHz.

This image was converted with the RLC model, the transmission line model and the Black Box calibration method. The results can be seen in Figure 3.21.

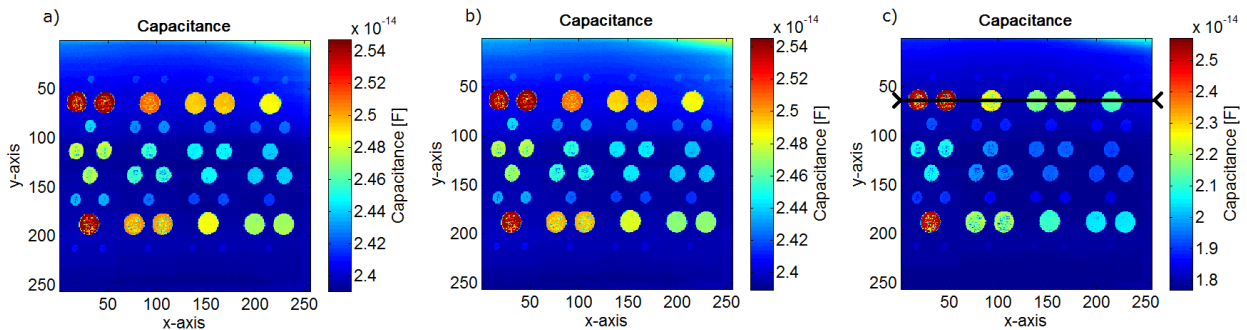


Figure 3.21: Capacitance values read out of the image conversion results of the RLC model (a), the transmission line model (b) and the Black Box calibration method (c).

On the very first sight the results look very similar. By taking a look at the scaling of the images one can recognize that RLC model and the transmission line model deliver almost the same results, but the span

of the values is shorter than in the Black Box result. This becomes clearer when taking a look at the horizontal cross section at line number 63 (Figure 3.22).

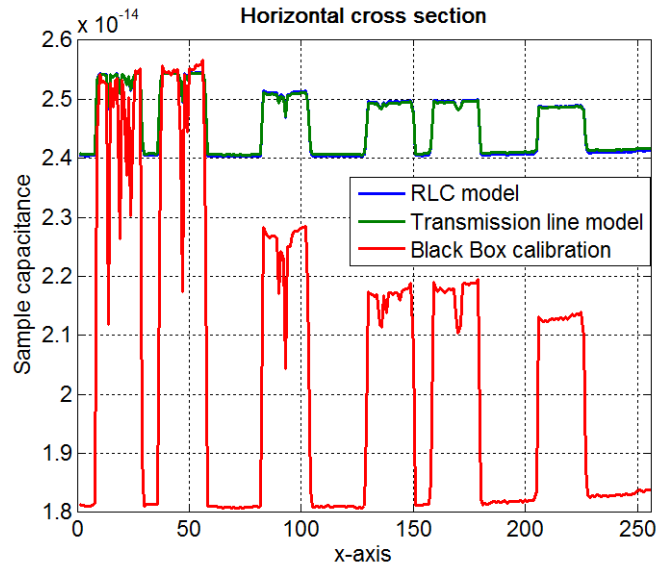


Figure 3.22: Horizontal cross section of Figure 3.21, line number 63.

This diagram shows that the capacitance value span of the Black Box calibration method is about five times higher than for the two models. This fact can be recognized all along this chapter. A discussion about this can be found in the conclusions of this chapter. As already mentioned, the frequency was performed at the biggest gold capacitor, that's why the capacitance values at the first two gold pads are the same at all three analysis methods.

The same procedure can be done with the sample resistance which is shown in Figure 3.23.

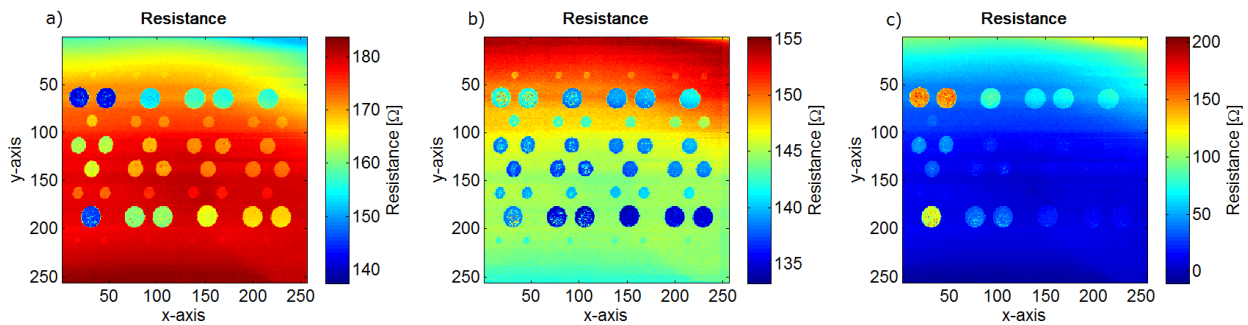


Figure 3.23: Resistance values according to the RLC model (a), the transmission line model (b) and the Black Box calibration method (c).

Again, a horizontal cross section at line number 63 gives better insight (Figure 3.24).

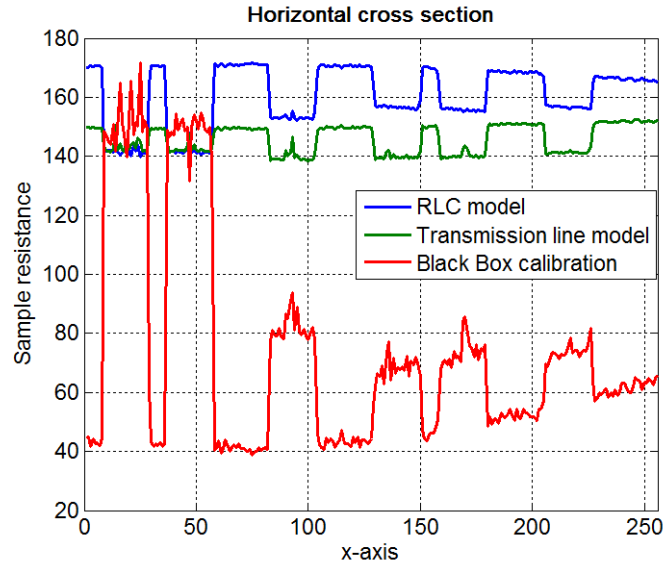


Figure 3.24: Horizontal cross section of Figure 3.23, line number 63.

The resistance value span of the Black Box calibration method again is five times higher than for the models. But this time, the two models deliver different values for the sample resistance. Also the curve characteristics are different. The Black Box method delivers a higher sample resistance at the gold capacitors as the simulation done by Georg Gramse suggests. But the results of the two models show a smaller sample resistance at the gold capacitors. Obviously the two models can not represent the sample resistance correctly. This fact has been recognized all along the analysis of the measurements, that's why the sample resistance will not be compared anymore.

But what can be compared are the capacitance values of the four capacitor sizes on the first oxide step. This allows a better comparison of the results at different measurement frequencies. We expect that the biggest capacitor has the same capacity no matter what model or what measurement frequencies were used because of the standardized conversion at the point where the frequency sweep was performed (Figure 3.25).

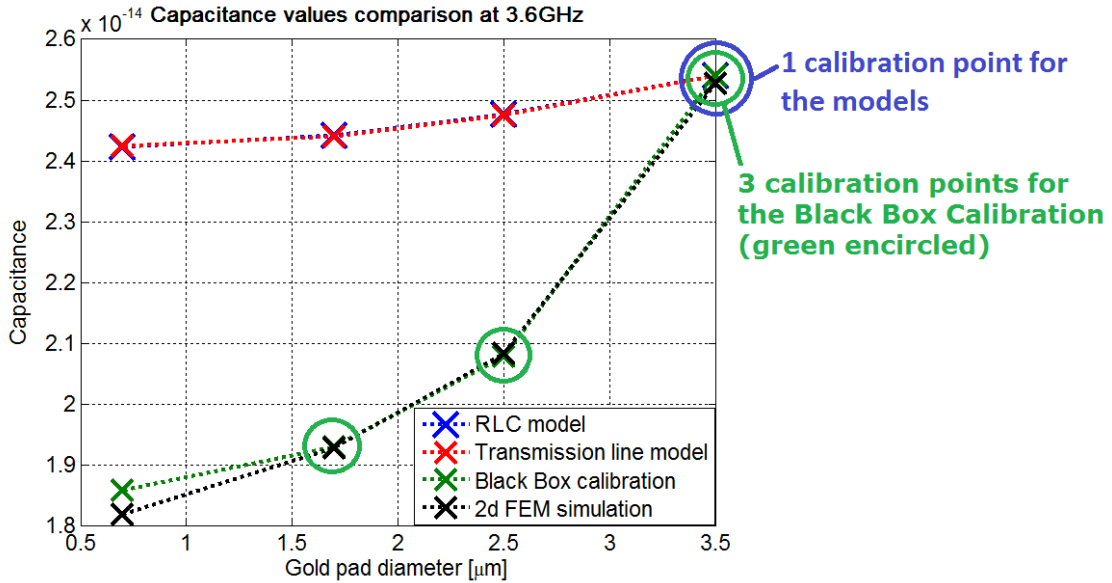


Figure 3.25: Capacitance values over the gold pad diameter at 3.652564GHz. Shown are the results of the RLC model, the transmission line model, the Black Box calibration method, the simulation results from Georg Gramse and the points the models use for calibration.

The Black Box calibrations results only are consistent with the simulation results because it uses three of the four capacitance values as calibration points.

The same diagram for other measurement frequencies show similar results and are shown in Figure 3.26 and in Figure 3.27.

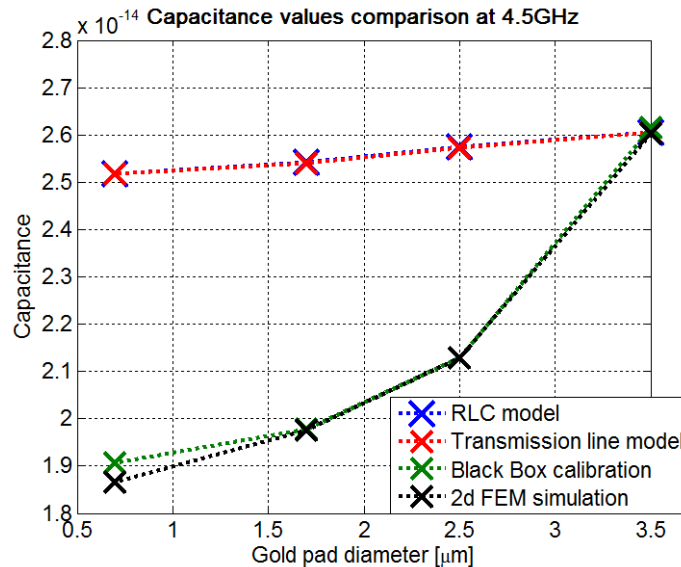


Figure 3.26: Capacitance values over the gold pad diameter at 4.55GHz. Shown are the results of the RLC model, the transmission line model, the Black Box calibration method and the simulation results from Georg Gramse.

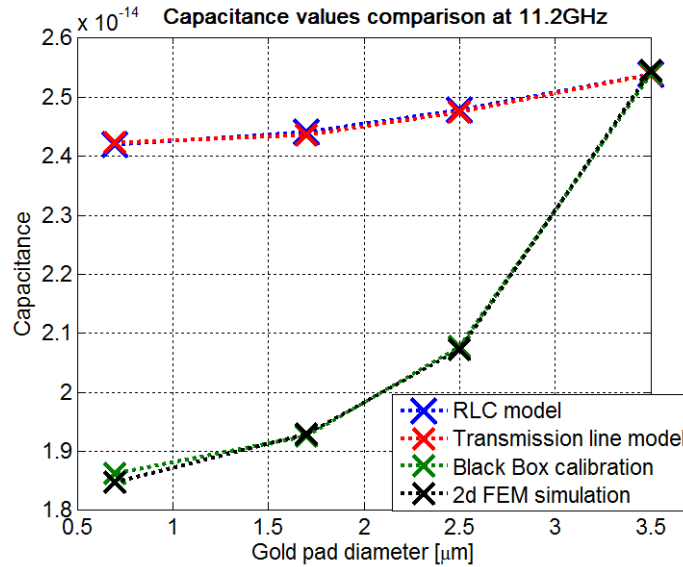


Figure 3.27: Capacitance values over the gold pad diameter at 11.201282GHz. Shown are the results of the RLC model, the transmission line model, the Black Box calibration method and the simulation results from Georg Gramse.

One can clearly recognize the similar curvature of all three analysis methods. Also the similarity of the two models is always present at any measurement frequency. A discussion about this can be found at the end of this chapter.

### 3.2.2 S11(V) curve conversion results

Due to the sweep adaption process mentioned in chapter 3.2 this chapter can concentrate on the analysis and visualization of the C(V) curves capacitance difference. The capacitance difference is the difference of the stationary values at the right and the left side of the C(V) curve. This is equal to the capacitance difference between the accumulation state and strong inversion state for n-doped semiconductors.

The first thing what needs to be checked is whether the small influence of the PNA Power has a big influence on the C(V) curves or not. Also, the influence of the exact measurement frequency according to chapter 1.1.3.4 will be investigated.

#### 3.2.2.1 Influence of the PNA power

The first PNA power sweep was performed at 3.6GHz. The converted capacitance voltage curves according to the RLC model and the transmission line model are shown in Figure 3.28 and Figure 3.29.

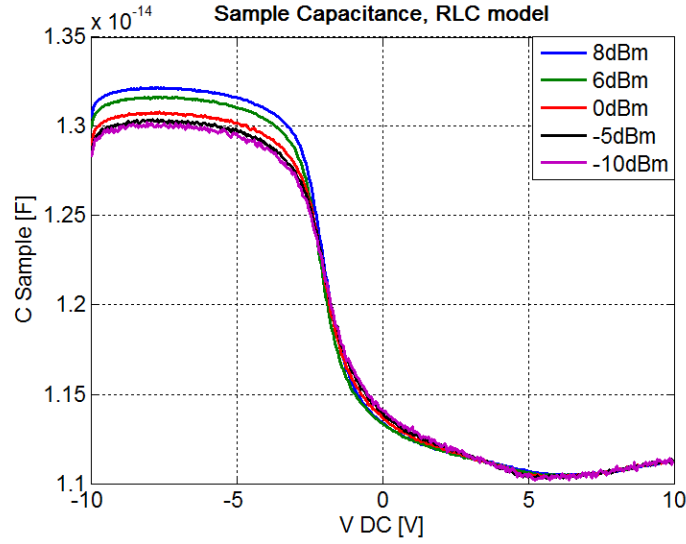


Figure 3.28: Capacitance voltage curves at 3.652564GHz with different PNA power according to the RLC model.

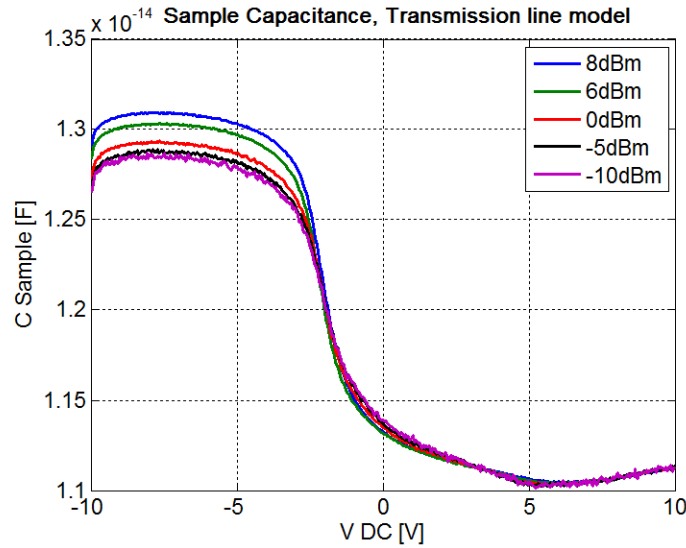


Figure 3.29: Capacitance voltage curves at 3.652564GHz with different PNA power according to the transmission line model.

The tabular form reveals more details.

Table 3.4: Capacitance differences at 3.652564GHz at different PNA power values according to the RLC model and the transmission line model.

PNA power [dBm]	Capacitance difference [F] RLC model	Capacitance difference [F] Transmission line model
8	$-2.08 \cdot 10^{-15}$	$-1.96 \cdot 10^{-15}$
6	$-2.03 \cdot 10^{-15}$	$-1.91 \cdot 10^{-15}$
0	$-1.95 \cdot 10^{-15}$	$-1.81 \cdot 10^{-15}$
-5	$-1.90 \cdot 10^{-15}$	$-1.76 \cdot 10^{-15}$
-10	$-1.88 \cdot 10^{-15}$	$-1.73 \cdot 10^{-15}$

The values change around 10% for both models. These values can also be plotted in a graph.

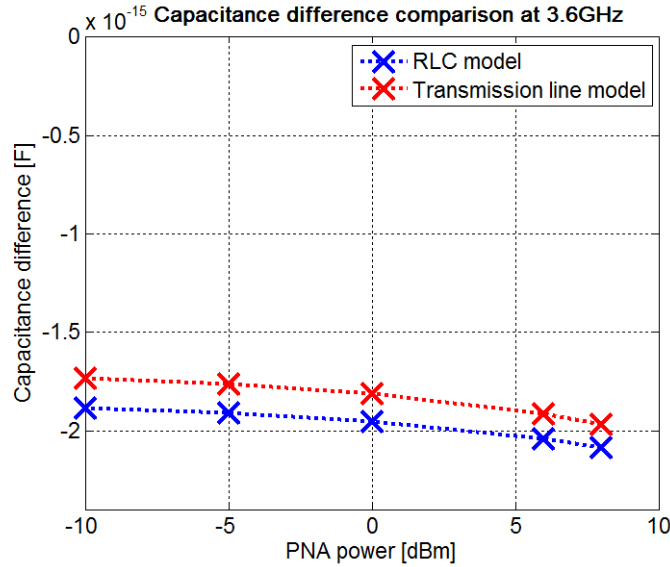


Figure 3.30: Capacitance difference over the PNA power at 3.652564GHz according to the RLC model and the transmission line model.

The theoretical capacitance difference according to the physical model is about  $5.58 \cdot 10^{-15} \text{F}$ . As the algebraic sign suggests both models deliver a curve progression in the wrong direction which means the capacitance isn't higher in the accumulation state (positive voltages) than in the depletion state (negative voltages). Also, the capacitance difference is too little compared to the physical model. At the end of this chapter a detailed discussion about the frequency dependency of the capacitance difference and algebraic sign can be found.

The capacitance analyses of the PNA power sweep measurements at 1.8GHz show very similar results.

Table 3.5: Capacitance differences at 1.824338GHz at different PNA power values according to the RLC model and the transmission line model.

PNA power [dBm]	Capacitance difference [F] RLC model	Capacitance difference [F] Transmission line model
8	$-1.084 \cdot 10^{-14}$	$-1.087 \cdot 10^{-14}$
6	$-1.075 \cdot 10^{-14}$	$-1.078 \cdot 10^{-14}$
0	$-1.060 \cdot 10^{-14}$	$-1.061 \cdot 10^{-14}$
-5	$-1.050 \cdot 10^{-14}$	$-1.050 \cdot 10^{-14}$
-10	$-1.045 \cdot 10^{-14}$	$-1.045 \cdot 10^{-14}$

The values change around 3.5% with decreasing PNA power for both models. The theoretical capacitance difference according to the physical model of about  $5.58 \cdot 10^{-15} \text{F}$  stays the same of course. So, the models deliver a two times higher difference than the theory predicts at 1.8GHz. The algebraic sign is wrong again. The values from Table 3.5 were plotted in Figure 3.31.

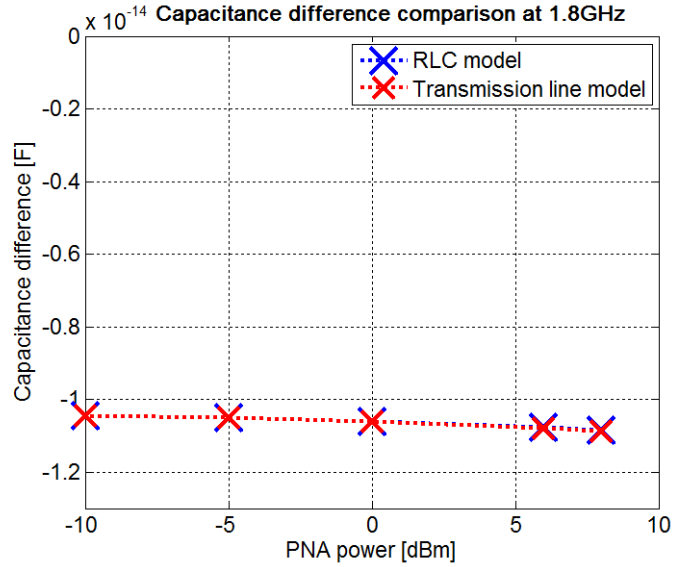


Figure 3.31: Capacitance difference over the PNA power at 1.824338GHz according to the RLC model and the transmission line model.

### 3.2.2.2 Influence of the distance between measurement frequency and resonance minimum

In chapter 1.1.3.4.2 the measurement frequency was varied around the resonance minimum at 3.6GHz and 1.8GHz, and S11(V) curves were recorded. Here, the influence of the exact measurement frequency around a resonance minimum on the capacitance difference will be investigated. Figure 3.32 shows the converted capacitance difference values at 3.6GHz.

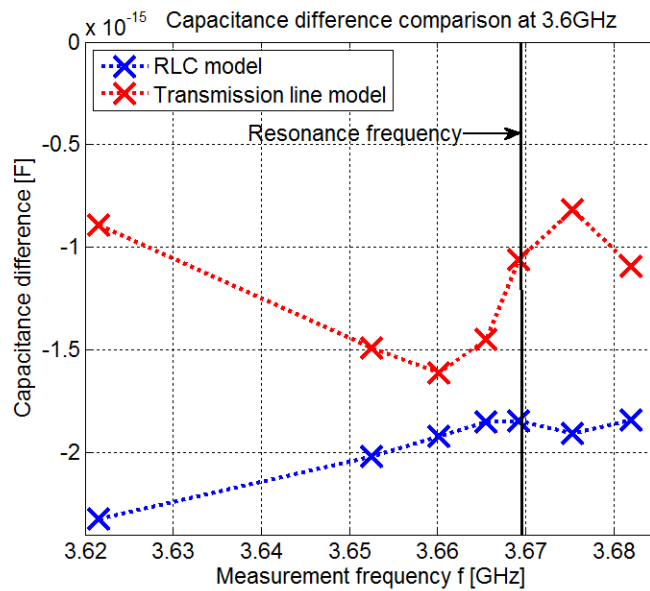


Figure 3.32: Capacitance difference over the measurement frequency around the resonance minimum at 3.66GHz according to the RLC model and the transmission line model.

Since the further measurements uniformly were made on the left side of the resonance minimum, the data points over 3.67GHz doesn't matter anymore. Below that frequency, the RLC model seems to deliver slightly more constant and uniform values.

The conversions of the measurements made around 1.8GHz are shown in Figure 3.33.

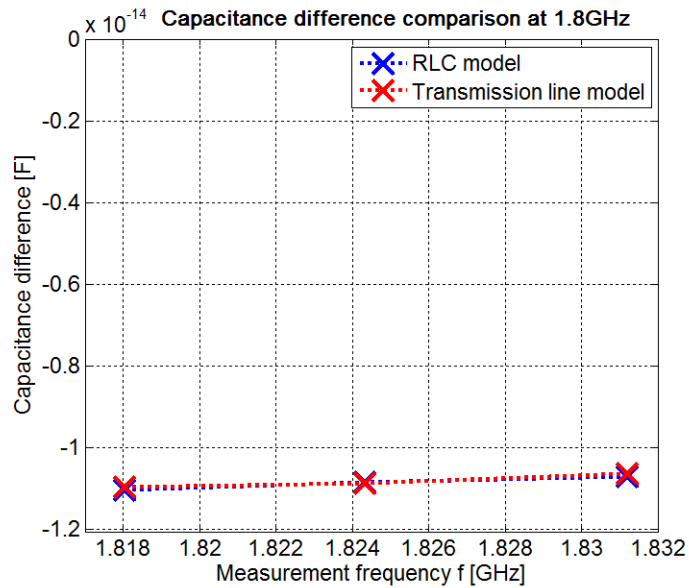


Figure 3.33: Capacitance difference values over the measurement frequency around the resonance minimum at 1.8GHz according to the RLC model and the transmission line model.

Both models deliver very similar and uniform values which nevertheless have the wrong algebraic sign and are too high compared to the theoretical capacitance difference of  $5.58 \cdot 10^{-15}$ F.

### 3.2.2.3 Recapitulation

The conversion of the measurements which were made to investigate the stability and the influence of certain measurement parameters has come to an end. There was no systematic scheme visible. The capacitance differences at 3.6GHz and at 1.8GHz show the wrong algebraic sign. The next subchapter will be more enlightening.

### 3.2.3 Investigation of the frequency dependency of the capacitance difference

S11(V) curves were measured at many different measurement frequencies on four different capacitor sizes. For each capacitor size the frequency dependency of the capacitance difference is shown in the following four images (Figure 3.34 to Figure 3.37). The results were discussed in the following conclusion chapter.

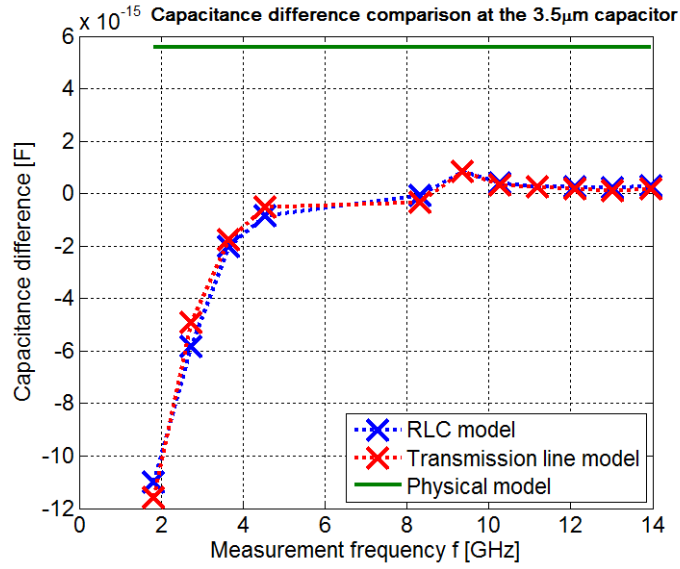


Figure 3.34: Capacitance difference over the measurement frequency at many different resonance minima according to the RLC model and the transmission line model. Also the theoretical values according to the physical model are shown (green). The measurements were made on the 3.5µm gold pad.

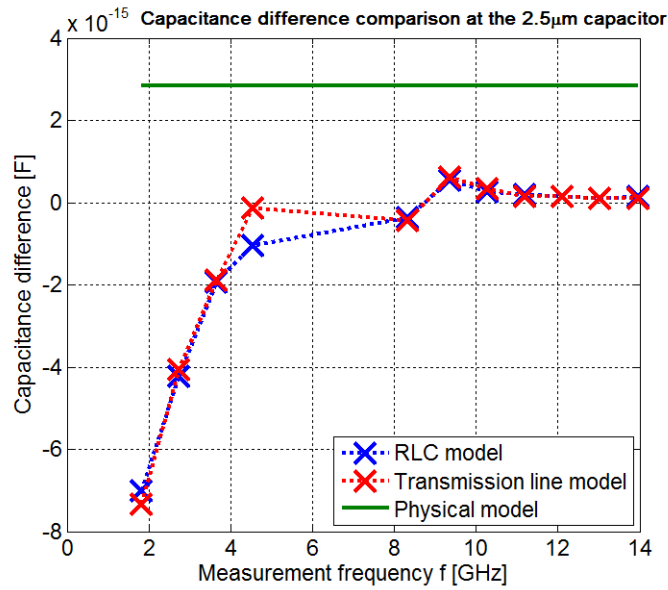


Figure 3.35: Capacitance difference over the measurement frequency at many different resonance minima according to the RLC model and the transmission line model. Also the theoretical values according to the physical model are shown (green). The measurements were made on the 2.5µm gold pad.

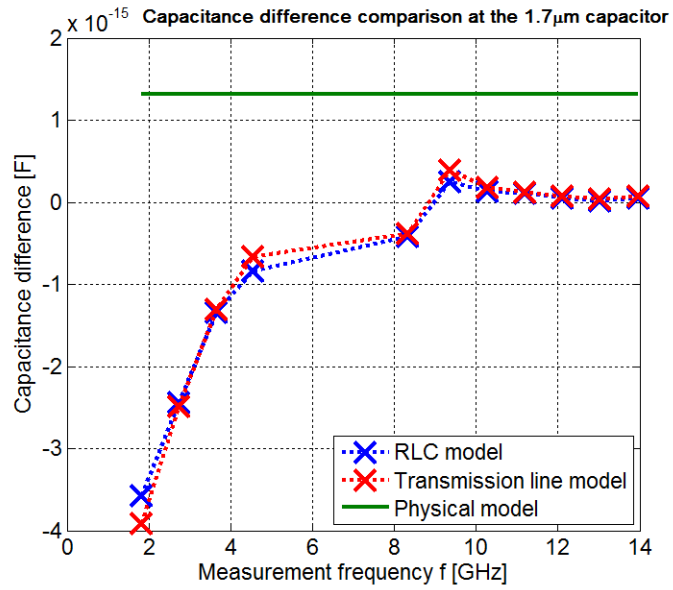


Figure 3.36: Capacitance difference over the measurement frequency at many different resonance minima according to the RLC model and the transmission line model. Also the theoretical values according to the physical model are shown (green). The measurements were made on the 1.7µm gold pad.

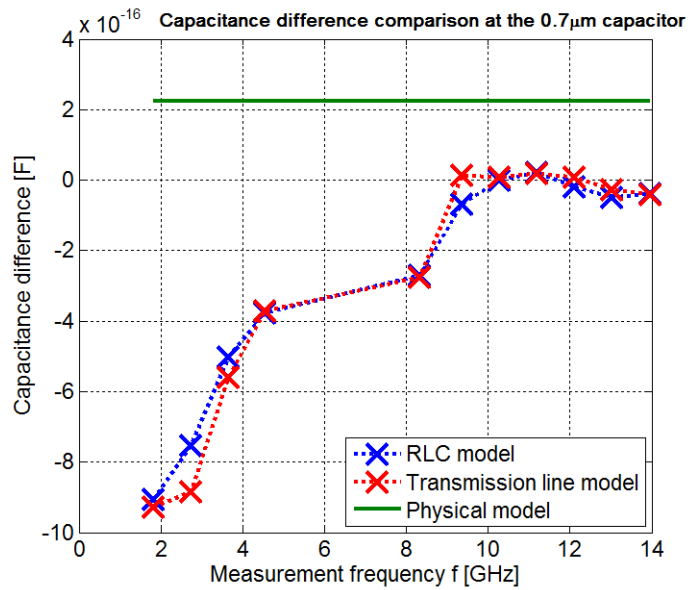


Figure 3.37: Capacitance difference over the measurement frequency at many different resonance minima according to the RLC model and the transmission line model. Also the theoretical values according to the physical model are shown (green). The measurements were made on the 0.7µm gold pad.

### 3.3 Recapitulation of the conversion results

Several images were transformed into capacitance and resistance values with both models and the Black Box calibration method. Also several  $S_{11}(V)$  curves were transformed into capacitance values with the models and compared to the theoretical values according to chapter 2.1. In these measurements certain settings were varied to find out how big the influence on the capacitance results is. These measurements were followed by systematically measurements at nearly every resonance minima between 1GHz and 14GHz. They also were transformed into capacitance values which gives insight into the frequency dependency of the resulting capacitance difference values of the  $C(V)$  curves.

One can recognize the same behaviour at every capacitor size. It is also eye-catching that both models nearly always give the same result which nevertheless is pretty different of the theoretical values. No matter what kind of measurement type one takes a look at, the models always show the same results in capacitance values which are always smaller than the values coming from the Black Box calibration method and the simulation. The similarity of the two models and the difference to the theoretical  $C(V)$  curves and the Black Box calibration lead to the speculation that maybe there is something unknown going on in the SMM which the models in this form can't handle. This leads to the thought that maybe some little adaption would increase the validity of the models. But different modelling attempts of adding some parasitic capacitance or resistance in series or parallel weren't successful.

## 4 Conclusion

The SMM setup was presented in the first chapter including a detailed explanation of the connection between the PNA and the AFM. Also how this connection influences the frequency sweep was illustrated. The short ripples in the frequency sweep were removed by using the E-Cal module. The last part of the first chapter was an investigation of the measured frequency sweep in the complex plane. After that, a physical model for MIS structures was invented. With the voltage induced band deflection it is possible to calculate the charge carrier density near the insulator semiconductor interface. Capacitance voltage curves on arbitrary MIS structures could be predicted. This physical model can handle the dimensions and different electrical properties of the sample, the dimensions and curvature of the tip and the gold pad structures. This was achieved by simplifying the complex structures into several MIS structures with an air gap if necessary. The accumulation, depletion and inversion state were analysed with the help of this model. Two further models were introduced which imitate the microwave behaviour of the SMM setup. The RLC model and the transmission line model use the frequency sweep for calibration. For the RLC model, a further phase adaption was invented. A deep analysis of the structure and the frequency behaviour including the sensitivity completes this chapter. The next topic was to level up the measurements done with the SMM on a reliable and uniform level. A guidance how to measure correct  $S_{11}(V)$  curves was presented. The reliability and the physical correctness of the measurements were tested by comparing the  $S_{11}(V)$  curves which were measured on different gold pad sizes, with different PNA power levels and with different measurement frequencies around a resonance minimum. After that, systematically measurements were performed at many different measurement frequencies.

The RLC model and the transmission line model were used to transform measured images and  $S_{11}(V)$  curves into capacitance values. The resulting capacitance values were compared with the results of the physical model and with the results of a 2d FEM simulation done by Georg Gramse. Due to a adaption procedure to eliminate the drift of the SMM setup, a concentration on the capacitance difference of the  $C(V)$  curves was possible. First, the influence of the PNA power and the exact measurement frequency around a resonance minimum on the capacitance difference was investigated. After that, the systematically measurements at many different frequencies were transformed into capacitance values too. It turned out that the two models deliver nearly always the same capacitance values at every measurement frequency. On the other hand the converted capacitance values and those from the physical model differ strongly. The models cannot describe the SMM setup correctly. Attempts to adapt the models in order to increase their physical validity weren't successful.

# References

- [1] S. M. Sze and K. K. Ng, *Physics of Semiconductor Devices*. John Wiley & Sons, Inc., 2007.
- [2] H.P. Huber, *Nanoscale Capacitance Measurements and Applications in Biology using Scanning Microwave Microscopy*, PhD thesis, Johannes Kepler University Linz, 2013.
- [3] J. Smoliner, H.P. Huber, M. Hochleitner, M. Moertelmaier, and F. Kienberger, „*Scanning microwave microscopy/spectroscopy on metal-oxide-semiconductor systems*“, J. Appl. Phys. 108, 064315 (2010).
- [4] Clarysse, T., et al., *Epitaxial staircase structure for the calibration of electrical characterization techniques*. Journal of Vacuum Science & Technology B: Microelectronics and Nanometer Structures, 1998. 16(1): p. 394-400.
- [5] Reznik, A.N. and V.V. Talanov, *Quantitative model for near-field scanning microwave microscopy: Application to metrology of thin film dielectrics*. Review of Scientific Instruments, 2008. 79(11): p. 113708.
- [6] J. Hoffmann, M. Wollensack, M. Zeier, J. Niegemann, H.P. Huber, F. Kienberger, „*A Calibration Algorithm for Nearfield Scanning Microwave Microscopes*“, Nanotechnology (IEEE-NANO), 2012 12th IEEE Conference on , vol., no., pp.1,4, 20-23 Aug. 2012
- [7] H. P. Huber, I. Humer, M. Hochleitner, M. Fenner, M. Moertelmaier, C. Rankl, A. Imtiaz, T. M. Wallis, H. Tanbakuchi, P. Hinterdorfer, P. Kabos, J. Smoliner, J. J. Kopanski, F. Kienberger , *Calibrated nanoscale dopant profiling using a scanning microwave microscope*, J. Appl. Phys. 111, 014301 (2012)
- [8] H. P. Huber, M. Moertelmaier, T. M. Wallis, C. J. Chiang, M. Hochleitner, A. Imtiaz, Y. J. Oh, K. Schilcher, M. Dieudonne, J. Smoliner, P. Hinterdorfer, S. J. Rosner, H. Tanbakuchi, P. Kabos, and F. Kienberger, *Calibrated nanoscale capacitance measurements using a scanning microwave microscope*, Rev. Sci. Instrum. 81, 113701 (2010)
- [9] I. Humer, C. Eckhardt , H. P. Huber , F. Kienberger , J. Smoliner, *Tip Geometry Effects in Dopant Profiling by Scanning Microwave Microscope*, J. Appl. Phys., J. Appl. Phys. 111, 044314 (2012)
- [10] I. Humer, H. P. Huber, F. Kienberger, J. Danzberger, J. Smoliner, *Phase and Amplitude Sensitive Scanning Microwave Microscopy/ Spectroscopy on Metal- Oxide- Semiconductor System*, J. Appl. Phys., 111, 074313 (2012)
- [11] A. Imtiaz, T. M. Wallis, S. H. Lim, H. Tanbakuchi, H. P. Huber, A. Hornung, P. Hinterdorfer, J. Smoliner, F. Kienberger, P. Kabos, *Frequency-Selective Contrast on Variably Doped p-type Silicon with a Scanning Microwave Microscope*, J. Appl. Phys., 111, 093727 (2012)

- [12] Lai, K., et al., *Calibration of shielded microwave probes using bulk dielectrics*. Applied Physics Letters, 2008. 93(12): p. 123105.
- [13] Matey, J.R. and J. Blanc, *Scanning capacitance microscopy*. Journal of Applied Physics, 1985. 57(5): p. 1437-1444.
- [14] Williams, C.C., et al., *Lateral dopant profiling with 200 nm resolution by scanning capacitance microscopy*. Applied Physics Letters, 1989. 55(16): p. 1662-1664.
- [15] Williams, C.C., et al., *Lateral dopant profiling on a 100 nm scale by scanning capacitance microscopy*. Journal of Vacuum Science & Technology A: Vacuum, Surfaces, and Films, 1990. 8(2): p. 895-898.
- [16] Kopanski, J.J., J.F. Marchiando, and J.R. Lowney, *Scanning capacitance microscopy applied to two-dimensional dopant profiling of semiconductors*. Materials Science and Engineering: B, 1997. 44(1-3): p. 46-51.
- [17] Isenbart, J., A. Born, and R. Wiesendanger, *The physical principles of scanning capacitance spectroscopy*. Applied Physics A: Materials Science & Processing, 2001. 72(8): p. S243-S251.
- [18] Stangoni, M.V., *Scanning Probe Techniques for Dopant Profile Characterization*, in Swiss Federal Institute of Technology, Zurich. 2005, University of Cagliari. p. 181.
- [19] Gao, C. and X.-D. Xiang, *Quantitative microwave near-field microscopy of dielectric properties*. Review of Scientific Instruments, 1998. 69(11): p. 3846-3851.
- [20] Markx, G.H. and C.L. Davey, *The dielectric properties of biological cells at radiofrequencies: applications in biotechnology*. Enzyme and Microbial Technology, 1999. 25(3-5): p. 161-171.
- [21] Huang, Y., C.C. Williams, and J. Slinkman, *Quantitative two-dimensional dopant profile measurement and inverse modeling by scanning capacitance microscopy*. Applied Physics Letters, 1995. 66(3): p. 344-346.
- [22] Xiang, X.D. and C. Gao, *Quantitative complex electrical impedance microscopy by scanning evanescent microwave microscope*. Materials Characterization, 2002. 48(2-3): p. 117-125.